^{182}W and HSE constraints from 2.7 Ga komatiites on the heterogeneous nature of the Archen mantle

Igor S. Puchtel[1*], Janne Blichert-Toft[2], Mathieu Touboul[1,2], and Richard J. Walker[1]

[1]Department of Geology, University of Maryland, College Park, MD 20742, USA
[2]Laboratoire de Géologie de Lyon, Ecole Normale Supérieure de Lyon and Université Claude Bernard Lyon 1, CNRS UMR 5276, 46 Allée d'Italie, 69007 Lyon, France

*Corresponding author: ipuchtel@umd.edu

Revised for:
Geochimica et Cosmochimica Acta

Final Version: November 27, 2017

Keywords: ^{182}Hf-^{182}W and ^{187}Re-^{187}Os isotopic systems, deficit in highly siderophile elements, Boston Creek komatiitic basalt lava flow, stochastic late accretion, sluggish mixing of the mantle

Abstract

While the isotopically heterogeneous nature of the terrestrial mantle has long been established, the origin, scale, and longevity of the heterogeneities with regard to different elements and isotopic systems are still debated. In this study, we report Nd, Hf, W, and Os isotopic and highly siderophile element (HSE) abundance data for the Boston Creek komatiitic basalt lava flow (BCF) in the 2.7 Ga Abitibi greenstone belt, Canada. This lava flow is characterized by strong depletions in Al and heavy rare earth elements (REE), enrichments in light REE, and initial $\varepsilon^{143}Nd = +2.5\pm0.2$ and $\varepsilon^{176}Hf = +4.2\pm0.9$ indicative of derivation from a deep mantle source with time-integrated suprachondritic Sm/Nd and Lu/Hf ratios. The data plot on the terrestrial Nd-Hf array suggesting minimal involvement of early magma ocean processes in the fractionation of lithophile trace elements in the mantle source. This conclusion is supported by a mean $^{142}Nd/^{144}Nd$ that is unresolvable from terrestrial standards. At the same time, the BCF exhibits a positive ^{182}W anomaly ($\mu^{182}W = +11.7\pm4.5$), yet is characterized by chondritic initial $\gamma^{187}Os = +0.1\pm0.3$ and low HSE abundances inferred for its mantle source (35±5% of those estimated for the present-day Bulk Silicate Earth, BSE). Collectively, these characteristics are unique among the Archean komatiite systems studied so far. The deficit in the HSE, coupled with the chondritic Os isotopic composition, but a positive ^{182}W anomaly, are best explained by derivation of the parental BCF magma from a mantle domain characterized by predominance of HSE-deficient, differentiated late accreted material. According to the model presented here, the mantle domain that gave rise to the BCF received only ~35% of the present-day HSE complement in the BSE before becoming isolated from the rest of the convecting mantle until the time of komatiite emplacement at 2.72 Ga. These new data provide strong evidence for the highly heterogeneous nature of the Archean mantle in terms of absolute HSE abundances and for its slow mixing, on a time scale of at least 1.7 billion years. Additionally, they are consistent with a stagnant-lid plate tectonic regime in the Hadean and Archean, prior to the onset of modern-style plate tectonics.

1. Introduction

While the isotopically heterogeneous nature of the terrestrial mantle has long been established, the origin, scale, and longevity of the heterogeneities with regard to different elements and isotopic systems are still debated. Some of the chemical heterogeneities may have been primordial, reflecting planetary accretion/differentiation and magma ocean crystallization processes, whereas others have definitively resulted from later processes associated with the dynamic regime of the planet, especially crustal recycling. The ^{142}Nd and ^{182}W anomalies found in some early Earth rocks likely formed within the first ~500 and ~50 Ma, respectively, of Earth's history, while ^{146}Sm and ^{182}Hf were still extant, as a result of early planetary differentiation event(s). The largest ^{142}Nd anomalies, ranging as high as +20 ppm and as low as −15 ppm, have been reported for the Eoarchean or older supracrustal rocks from the Isua greenstone belt, Greenland (Boyet *et al.*, 2003; Caro *et al.*, 2003; Boyet and Carlson, 2005; Boyet and Carlson, 2006; Caro *et al.*, 2006; Bennett *et al.*, 2007; Rizo *et al.*, 2011; Rizo *et al.*, 2012; Rizo *et al.*, 2013), the Nuvvuagittuq greenstone belt, Québec (O'Neil *et al.*, 2008; O'Neil *et al.*, 2012; Roth *et al.*, 2013), and the Ukaliq supracrustal belt, Québec (Caro *et al.*, 2017). Few terrestrial samples younger than 3.5 Ga are known to have μ^{142}Nd values deviating from terrestrial standards by more than ±3 ppm (Rizo *et al.*, 2012; Debaille *et al.*, 2013). Similarly, positive ^{182}W anomalies as high as +23 ppm have been reported for supracrustal rocks from Greenland and Québec (Willbold *et al.*, 2011; Touboul *et al.*, 2014; Dale *et al.*, 2017), as well as from the Northwest Territories (Willbold *et al.*, 2015) and Fennoscandia (Puchtel *et al.*, 2016b).

The apparent disappearance of ^{142}Nd anomalies during the Archean was initially interpreted as evidence for re-homogenization of early-formed silicate reservoirs within the mantle on the time scale of at least one billion years (Caro *et al.*, 2006; Bennett *et al.*, 2007; Carlson and Boyet, 2008). The presence of sizeable isotopic anomalies in late Archean and

younger rocks, however, indicates that mantle mixing did not completely eliminate primordial anomalies early in Earth history. The ~15 ppm positive ^{182}W anomalies found in the 2.82 Ga Kostomuksha komatiites were interpreted to indicate that early-formed domains in the mantle survived for at least 1.7 Ga (Touboul *et al.*, 2012), while ^{182}W isotopic heterogeneities in the Phanerozoic, including modern rocks from Baffin Bay, Ontong Java, Hawaii, and Samoa suggest that primordial domains are still present in the mantle (Rizo *et al.*, 2016a; Mundl *et al.*, 2017).

Some of the inefficient mixing evidenced by the longevity of primordial domains could be due to early Earth tectonic regimes differing from those of modern-style plate tectonics (O'Neill and Debaille, 2014). For example, the survival of ^{142}Nd anomaly of +7±3 ppm in 2.72 Ga tholeiites from the Abitibi greenstone belt (AGB), but complete absence of ^{142}Nd anomalies in post-Archean record has been interpreted to indicate a global-scale transition from a stagnant-lid tectonic regime prior to 2.5 Ga to mobile-lid post-Archean plate tectonics (Debaille *et al.*, 2013).

Osmium isotope and highly siderophile element (HSE) abundance systematics provide additional information about early Earth processes. For example, the observation that the HSE occur in roughly chondritic relative proportions in the Bulk Silicate Earth (BSE), and that absolute abundances of at least some of the HSE are higher than would be expected from metal-silicate equilibration, have led to the concept of late accretion. Late accretion is commonly envisioned as a process whereby at least 0.5% of Earth's mass was added to the mantle through the continued accretion of planetesimals, subsequent to the cessation of core formation (Chou *et al.*, 1983; Morgan, 1985). Issues related to late accretion are much debated, including the composition of the late accreted materials and the time frame within which they were delivered to Earth and homogenized within the mantle (*e.g.,* (Maier *et al.*, 2009; Walker, 2014). Some of the uncertainties stem from the fact that the absolute HSE

114 abundances in the early Earth's mantle are not well constrained, and the causes of their
115 abundance variations are poorly understood. For example, on the basis of measured Pt
116 contents in Archean komatiites, (Maier *et al.*, 2009) argued for a gradual increase in HSE
117 abundances in their presumed deep mantle sources between ~3.5 and ~2.9 Ga, due to slow
118 downward mixing of a "late veneer" of chondritic materials.
119 In this study, we report combined ^{182}Hf-^{182}W, ^{146,147}Sm-^{142,143}Nd, ^{176}Lu-^{176}Hf, ^{187}Re-^{187}Os,
120 and HSE and lithophile trace element abundance data for 2.72 Ga komatiitic basalts from
121 Boston Creek Township in the AGB. We use the data to (1) constrain the long-term evolution
122 of the mantle domain beneath the Superior Craton that gave rise to the BCF parental magmas,
123 (2) evaluate the degree of late Archean mantle heterogeneity in terms of absolute HSE
124 abundances, based on our previously published and new HSE data, and (3) provide new
125 constraints on the timing of late accretionary processes and mixing times of the Earth's
126 mantle.

127 **2. Geological background, samples, and previous studies**

128 The geology, petrology, and geochemistry of the Boston Creek Flow (BCF) are described
129 in detail by (Stone *et al.*, 1987; Stone *et al.*, 1995a; Stone *et al.*, 1995b) and (Walker and
130 Stone, 2001). The BCF is located in the Ontario portion of the AGB, ~16 km south of
131 Kirkland Lake. Lavas of the AGB are interpreted to have been formed during three volcanic
132 cycles (Cycles I through III: (Jensen and Pyke, 1982). A complete volcanic cycle consisted of
133 a basal komatiite sequence, overlain by a tholeiitic sequence, followed by a calc-alkaline
134 sequence, and capped by an alkaline felsic sequence. The BCF belongs to Cycle II, which is
135 16 km thick and is composed of the komatiitic Wabewawa Group, the tholeiitic Catherine
136 Group, and the calc-alkaline Skead Group; the BCF is located at the top of the Wabewawa
137 Group. A differentiated tholeiitic flow at the base of the Catherine Group, immediately above
138 the BCF, has a U-Pb zircon age of 2720±2 Ma (Corfu and Noble, 1992). This age is

interpreted as the age of the entire tholeiitic succession and the BCF, and is similar to the age of komatiites from Munro Township in the northern part of the AGB of 2714±2 Ma (Corfu and Noble, 1992).

All Cycle II rocks have been regionally metamorphosed to the prehnite-pumpellyite facies, but portions of the Wabewawa Group, including the BCF, were later contact-metamorphosed to the greenschist facies during intrusion of the Round Lake Batholith (Jolly, 1980). The flow can be traced along strike for ~4.6 km, and its thickness varies between 45 and 115 m. Samples for this study were collected across the section of the flow exposed near O'Donald Lake, where it is ~100 m thick. In the study area, the flow is subdivided into the upper clinopyroxene spinifex-textured zone and the lower olivine-pyroxene-chromite-titanomagnetite cumulate zone (Fig. 1). The olivine cumulate subzone is ~33 m thick and consists largely of olivine grains 1-3 mm in size completely pseudomorphically replaced by serpentine and magnetite in a matrix of intercumulus pyroxene which itself is partly replaced by tremolite and chlorite. Chromite occurs as euhedral grains up to 1 mm in size either interstitial to or as inclusions in olivine. The upper part of the cumulate zone is occupied by the subzone of olivine-pyroxene cumulate ~7 m thick in the form of equigranular medium-grained rock consisting of pyroxene and olivine grains in a fine-grained matrix of plagioclase, chlorite, actinolite, and opaques. The contact between the cumulate zone and overlying coarse-grained basalt subzone of the spinifex zone is marked by a sharp increase in the proportion of plagioclase. The basalt consists of euhedral grains of clinopyroxene and subhedral grains of plagioclase and titanomagnetite submerged in a groundmass of chlorite, actinolite, plagioclase, epidote and calcite. Further up in the spinifex zone, the coarse-grained basalt subzone is replaced by a subzone of coarse random pyroxene spinifex, then by columnar pyroxene spinifex, and, finally, by fine random pyroxene spinifex at the top of the flow. Most of the spinifex zone above the basalt subzone consists of column-shaped

amphibole pseudomorphs after skeletal clinopyroxene grains up to 100 mm long and 0.5-2.0 mm wide oriented subperpendicular to the flow boundaries in a matrix of fine-grained plagioclase, chlorite, amphibole, and opaques. At the top and bottom of the spinifex zone, the amphibole pseudomorphs after clinopyroxene are smaller and randomly oriented. In addition, the top of the spinifex-textured zone lacks plagioclase and has a higher proportion of what was once glassy material.

The BCF is unique in having an FeO content of the emplaced lava as high as 17 wt. %, strong depletions in Al and heavy rare earth elements (REE), and enrichments in light REE and other highly incompatible lithophile trace elements (Stone *et al.*, 1987; Stone *et al.*, 1995a). Rocks from this flow were also shown to be characterized by initial ε^{143}Nd of *ca.* +2.5 (Stone *et al.*, 1995a) and γ^{187}Os of −3.8±0.5 (Walker and Stone, 2001).

Samples for this study were collected across the BCF (Fig. 1) to attain the largest possible compositional range among individual samples necessary for obtaining a Re-Os isochron and estimating the absolute HSE abundances in its mantle source. The purpose of the new sampling campaign was to collect high-quality material using exclusively metal-free equipment and, with that, to acquire high-precision ^{187}Re-^{187}Os, ^{176}Lu-^{176}Hf, ^{146,147}Sm-^{142,143}Nd, ^{182}W isotopic and lithophile trace element, HSE, and W abundance data.

3. Analytical techniques

3.1. Sample preparation

The samples between 1.0 and 2.0 kg in weight were collected from the surface outcrops using a sledge hammer and cut into rectangular 0.5”×2.0”×3.0” slabs using a diamond saw to remove any sledge hammer marks and signs of alteration. The slabs were then polished on all sides using SiC sandpaper to remove the saw marks, rinsed with milli-Q water, and crushed in an alumina-faced jaw crusher. Small slabs were cut off and used to prepare polished thin sections. A 200-g aliquot of each crushed sample was ground in an alumina shatter box and then finely re-ground in an alumina-faced disk mill. This ground material was used for the chemical studies.

3.2. Major, minor, trace element, and transition metal abundances

Major and minor element analyses were carried out at the Franklin and Marshall College on fused glass discs using a Phillips 2404 XRF vacuum spectrometer and following the protocol of (Mertzman, 2000). Typical accuracy of the analyses was ~2% relative for major elements present in concentrations greater than 0.5% and ~5% relative for the rest of the major and the minor elements as determined via analysis of the USGS GRM BIR-1, BCR-1, and BHVO-2 as unknowns (Table 1).

The abundances of the trace elements were determined using the standard addition solution inductively-coupled plasma mass-spectrometry technique (SA ICP-MS) following the protocol outlined in (Puchtel *et al.*, 2016b). Between 25 and 35 mg of sample powder were weighed out in 15 mL screw-cap Savillex Teflon vials. Approximately 0.5 mL double-distilled concentrated HNO_3 and 3 mL double-distilled concentrated HF were added, the vials were sealed and kept on a hotplate at 200ºC for 48 hours. The vials were then opened, the sample solutions evaporated to dryness, 0.5 mL of distilled SeaStar concentrated $HClO_4$ added to the dry residue to convert fluorides into perchlorates, the vials sealed again and kept on a hotplate at 200ºC for 48 hours. The vials were re-opened and the sample solutions dried down on the hotplate at 230ºC. This step was followed by re-dissolution of the residue in 2 mL of 6*M* HCl to convert it into the chloride form. This step was repeated. The dry residue was taken up in ~10 grams of 0.8*M* HNO_3 (with the exact weight recorded), and this stock solution was used for preparing spiked aliquots used for ICP-MS measurements. Two standard addition spikes were prepared, one containing concentrated mixed solutions of Y and Zr, and the other containing Nb, Hf, Th, U, and REE. Three aliquots of each sample, each containing ~1.0 gram of sample stock solution (with the exact weight recorded), were prepared for each of the two groups of the elements to be analyzed, one containing no spike, one with the amount of spike containing 2× the estimated amount of element present in the sample aliquot, and one with the amount of spike containing 4× the estimated amount of element present in the sample aliquot, with the exact weights of the spikes recorded. One total analytical blank (TAB) was also prepared and measured with every batch of six samples. Approximately 100 mg (with the exact weight recorded) of 500 ppb In solution was added to each sample aliquot and the TAB solutions to monitor and correct for signal drift during analysis, and the one sample- and two sample-spike solutions for each sample were diluted to 10 grams with 0.8*M* HNO_3.

The sample solutions were analyzed on a *ThermoFisher Element2* sector field ICP-MS at the *Plasma Laboratory (PL)*, University of Maryland. Prior to analysis, the instrument was

thoroughly tuned to maximize sensitivity and minimize oxide production, and mass-calibrated. The intensities of selected isotopes of each element were measured in either low resolution (lithophile trace elements) or medium resolution (transition metals) modes. The raw data were reduced using an in-house Excel macro. The in-run uncertainties on the concentrations were typically better than 1% for all elements (2SE). The accuracy and precision of the analyses were determined via replicate analysis of the USGS GRM BIR-1 and BCR-1 (Puchtel *et al.*, 2016b); for most elements, it was ~5% (2SD), which includes the uncertainty introduced by the SRM powder heterogeneity.

3.3. Re-Os isotopic compositions and HSE abundances

To obtain the Re-Os isotopic and HSE abundance data, ca. 1.5 g whole-rock powder, 6 mL purged, triple-distilled concentrated HNO_3, 4 mL triple-distilled concentrated HCl, and appropriate amounts of mixed ^{185}Re-^{190}Os and HSE (^{99}Ru,^{105}Pd,^{191}Ir,^{194}Pt) spikes were sealed in double internally-cleaned, chilled 25 mL Pyrex™ borosilicate Carius Tubes (CTs) and heated to 270°C for 96 h. Osmium was extracted from the acid solution by CCl_4 solvent extraction (Cohen and Waters, 1996), back-extracted into HBr, and purified via microdistillation (Birck et al., 1997). Ruthenium, Pd, Re, Ir, and Pt were separated and purified using anion-exchange chromatography following a modified protocol of (Rehkämper and Halliday, 1997).

Osmium isotopic measurements were done *via* negative thermal ionization mass spectrometry (N-TIMS: (Creaser *et al.*, 1991). All samples were analyzed using a secondary electron multiplier (SEM) detector of a *ThermoFisher Triton* mass spectrometer at the *Isotope Geochemistry Laboratory (IGL),* University of Maryland. The measured isotopic ratios were corrected for mass fractionation using $^{192}Os/^{188}Os = 3.083$. The internal precision of measured $^{187}Os/^{188}Os$ for all samples was between 0.03% and 0.05% relative. The $^{187}Os/^{188}Os$ ratio of 300-500 pg loads of the in-house *Johnson-Matthey* Os standard measured during the two-year period leading up to the current analytical sessions averaged 0.11376±10 (2SD, $N = 64$). This value characterizes the external precision of the isotopic analyses (0.10%), which was used to estimate the true uncertainty on the measured $^{187}Os/^{188}Os$ ratio for each individual sample. The measured $^{187}Os/^{188}Os$ ratios were further corrected for instrumental mass bias relative to the average $^{187}Os/^{188}Os = 0.11379$ measured for the Johnson-Matthey Os standard on the Faraday cups of the *IGL Triton* (Puchtel *et al.*, 2016b). The correction factor of 1.00026 was calculated by dividing this value by the average $^{187}Os/^{188}Os$ measured for the *Johnson-Matthey* Os standard on the SEM of the same instrument.

The measurements of Ru, Pd, Re, Ir, and Pt were performed at the *PL* via ICP-MS using a *Nu Plasma* instrument with a triple electron multiplier configuration in static mode. Isotopic mass fractionation was monitored and corrected for by interspersing samples and standards. The accuracy of the data was assessed by comparing the results for the reference materials UB-N and GP-13 with results from other laboratories (Puchtel et al., 2014). In this study, we also analyzed several additional reference materials, including IAG MUH-1 (Austrian harzburgite), IAG OKUM (Ultramafic rock) and NRC TDB-1 (Diabase PGE Rock Material); these data are reported in Table 2, together with the reference values. MUH-1 and OKUM have compositions similar to the BCF cumulate samples with high Os, Ir, and Ru abundances, whereas TDB-1 is similar to the spinifex-textured samples with low Os, Ir, and Ru abundances. Concentrations of all HSE and Os isotopic compositions obtained at the *IGL* are in good agreement with the certified reference values. Diluted spiked aliquots of iron meteorites were run during each analytical session as secondary standards. The results from these runs agreed within 0.5% for Re and Ir, and within 2% for Ru, Pt, and Pd, with fractionation-corrected values obtained from measurements of undiluted iron meteorites using Faraday cups on the same instrument with a signal of >100 mV for the minor isotopes. Blank contributions were less than these values for the respective elements. The average TAB during the analytical campaign was (in pg): Ru 4.2, Pd 5.3, Re 0.28, Os 0.43, Ir 0.47, and Pt 95 ($N = 3$). The average TAB constituted less than 0.1% for Os for the majority of samples except for those with low Os abundances, for which it varied between 0.2 and 0.7%, less than 0.5% for Re, Ir, Ru, and Pd, and less than 2% for Pt of the total element analyzed in the samples. We therefore cite ±0.1 to ±0.7% as the uncertainty on the concentrations of Os, ±2% as the uncertainty on the concentrations of Ru, Pt, and Pd, and ±0.5% as the uncertainty on the concentrations of Re and Ir. The uncertainty on the Re/Os ratio was calculated for each particular sample via multiplying the uncertainties on the Re and Os abundances for this sample. These uncertainties vary between 0.6 and 1.1% relative.

The regression calculations were performed using ISOPLOT 3.00 (Ludwig, 2003). The uncertainties on the concentrations and isotopic ratios used for the regression calculations are those stated above. The initial $\gamma^{187}Os$ values were calculated as the per cent deviation of the isotopic composition at the time defined by the Re-Os isochron relative to the chondritic reference of (Shirey and Walker, 1998) at that time.

The average chondritic Os isotopic composition at the time defined by the isochron was calculated using the ^{187}Re decay constant $\lambda = 1.666\times10^{-11}$ year^{-1}, an early Solar System initial

$^{187}Os/^{188}Os = 0.09531$ at $T = 4558$ Ma, and $^{187}Re/^{188}Os = 0.40186$ (Smoliar *et al.*, 1996; Shirey and Walker, 1998).

3.4. Tungsten isotopic compositions and abundances

The W isotope and concentration measurements were carried out at the *IGL* following the chemical procedures described in (Touboul *et al.*, 2014) for purifying W, and measurement techniques developed by (Touboul and Walker, 2012) for determining W isotope compositions. For each isotopic analysis, between 2 and 5 grams of sample powder was processed to obtain the ~1 μg of W necessary for high-precision W isotope measurements. The sample powders were digested in 60 mL Savillex Teflon screw-cap vials using a 5:1 mixture of double-distilled concentrated HF and HNO_3 on a hot plate at 150°C for one week and dried down. The residues were digested in a mixture of 20 mL concentrated HNO_3 and 0.1 mL H_2O_2 at 120°C for 24 hours and dried down. This step was repeated. The residues were converted into the chloride form by repeated dissolutions in double-distilled 6*M* HCl and subsequent dry downs. The residues were finally re-dissolved in 10 mL of a mixture of 1*M* HCl and 0.1*M* HF. The sample solutions were centrifuged and the W in the supernatant was separated and purified using the four-stage ion-exchange chromatography protocol described in (Touboul and Walker, 2012), with minor modifications. The third stage involving a 1.5 mL anion-exchange column was repeated to improve the separation of Ti from W, which significantly increased W ionization efficiency. Tungsten recovery using this procedure was better than 90% for all samples analyzed.

Tungsten isotopic compositions were measured by N-TIMS on the *ThermoFisher Triton* mass-spectrometer at the *IGL* using a 2-line multi-static acquisition protocol and following the technique described by (Touboul and Walker, 2012). This technique relies on a double-normalization procedure for correcting the W isotope fractionation (using the $^{186}W/^{183}W$ ratio and an exponential law) and O isotope fractionation (using the $^{183}W/^{184}W$ ratio and a linear law). In contrast to a more recent analytical technique developed by (Archer *et al.*, 2017), where the O isotopic composition is determined during the analysis, our technique does not provide independent $^{183}W/^{184}W$ data. The long-term external precision (2SD) of the analysis was ±4.5 ppm on the $^{182}W/^{184}W$ ratio based on multiple measurements of the *Alfa Aesar* W standard solution. At the end of the useful life of the Faraday cups of the *Triton*, the external reproducibility tended to slightly increase, as the $^{182}W/^{184}W$ ratios started to drift. During the entire duration of the present analytical campaign (from 02/2013 through 11/2014), this decrease in the external reproducibility was observed in 03/2014 and 06/2014, after which the

Faraday cups were immediately replaced. For the samples measured in 03/2014 and 06/2014, the $\mu^{182}W$ values were calculated relative to the average $^{182}W/^{184}W$ ratios of the *Alfa Aesar* W standard measured in 03/2014 (magazines 324 and 325) and 06/2014 (magazines 326 and 327). For the rest of the samples, the $\mu^{182}W$ values were calculated relative to the long-term average $^{182}W/^{184}W$ ratios measured in the *Alfa Aesar* W standard between 02/2013 and 11/2014 (magazines 264 to 313 and 340 to 342).

Total procedural blanks averaged ~1.8 ng, which was less than 0.2% of the total W present in the analyzed W cuts. Blank corrections on the measured W isotope composition, therefore, were negligible.

Tungsten abundances were determined by isotope dilution ICP-MS. Between 100 and 200 mg of sample powder and a ^{182}W-enriched spike were equilibrated in 15 mL screw-cap *Savillex* Teflon vials using a 5:1 mixture of double-distilled concentrated HNO_3 and HF at 180ºC for 3-4 days, followed by the dry down of the solutions. Residues were treated with double-distilled concentrated HNO_3 and traces of H_2O_2 at 120ºC for 24 hours. After evaporation to dryness, residues were converted into the chloride form by adding 6*M* HCl, followed by another dry down. Residues were then equilibrated with a 6*M* HCl-0.01*M* HF mixture at 120ºC for ~24 h, after which complete dissolution usually was achieved. Finally, solutions were dried down and residues re-dissolved in 2 mL of a 0.5*M* HCl + 0.5*M* HF mixture, and W purified using a previously established anion-exchange chromatography technique (*e.g.,* (Kleine *et al.*, 2004a).

The W isotopic compositions of the spiked samples were measured using the *Nu Plasma* ICP-MS at the *PL*. The total analytical blank for W averaged 170±50 pg, corresponding to contributions of <1% of the total W present in the samples.

3.5. Sm-Nd isotopic compositions and abundances

The Sm-Nd isotopic studies were carried out at the *IGL* following the techniques outlined in (Puchtel *et al.*, 2016a). Between 200 and 300 mg of sample powder for each sample were tightly sealed with Teflon tape in a screw-cap 15 mL *Savillex* Teflon vial with 5 mL double-distilled concentrated HF and 1 mL double-distilled concentrated HNO_3 and digested on a hotplate at 200°C for 24 hours. The vessels were opened, the solutions dried down, new batches of acids added, and the digestion step was repeated at 200°C for 48 hours. After the solutions were again dried down, 0.5 mL of concentrated *SeaStar* $HClO_4$ were added, the vials sealed and kept on a hotplate at 200°C for 24 hours. The solutions were then dried down at ~230°C, and the residues converted into the chloride form using 6*M* HCl. This step was

repeated twice. The residue was then taken up in 5 g of 2.5*M* HCl (with the exact weight recorded) and a ~3% aliquot of the sample solution was weighed out (with the exact weight recorded) and used for determination of the $^{147}Sm/^{144}Nd$ ratios via the SA ICP-MS technique (without a knowledge of the precise weight of the sample represented by the amount of the sample aliquot, only the Sm/Nd ratios were determined). From the remaining sample solution, REE were first separated from the silicate matrix using standard cation-exchange chromatography. The Nd fractions were further separated from the other REEs using first 2-methyllactic acid cation-exchange chromatography and then HDEHP chromatography. The resultant Nd cuts were used for high-precision measurements of the Nd isotopic compositions.

Measurements of the Nd isotopic compositions were performed on the *ThermoFisher Triton* mass-spectrometer at the *IGL*, using a two-line acquisition protocol and a multi-dynamic routine. For each sample load, between 2400 and 3600 ratios were collected with 8 *sec*. integration times in blocks of 20 ratios each. For every three blocks of data collection, the two peaks were centered, the ion beam was re-focused, and the amplifiers were electronically rotated relative to the Faraday cup detectors. A 30 sec. baseline measurement per block was performed for each Faraday cup/amplifier pair by beam deflection. The effects of instrumental mass fractionation were corrected relative to $^{146}Nd/^{144}Nd = 0.7219$ using an exponential law. A total of 10 loads of 900 ng of the Nd standard AMES were run at the beginning and end of the analytical session, with 2400 ratios collected during each measurement. During the measurements, the signal intensities for both the standards and the samples were kept at constant levels, between 3V and 5V on the ^{142}Nd mass. The calculated $^{147}Sm/^{144}Nd$ ratios were between 10^{-5} and 10^{-6}, meaning that corrections for Sm isobaric interferences were negligible. The calculated $^{142}Ce/^{142}Nd$ ratios were between 10^{-5} and 10^{-4}, resulting in interference corrections of >10 ppm on the $^{142}Nd/^{144}Nd$ ratio in some samples. No correlation between measured $^{142}Nd/^{144}Nd$ and the intensity of the ^{140}Ce signal was observed, indicating that these interferences were adequately corrected for. During the course of the present analytical campaign, the external reproducibility of the AMES Nd standard solution measurements was ±2.8 ppm for $^{142}Nd/^{144}Nd$ and ±3.5 ppm for $^{143}Nd/^{144}Nd$ (2SD, $N = 34$). The $^{142}Nd/^{144}Nd$ ratios are expressed in $\mu^{142}Nd$ units calculated as part per million (ppm) deviations from the average $^{142}Nd/^{144}Nd$ ratio of the AMES Nd standard obtained during the course of the analytical campaign.

The $^{147}Sm/^{144}Nd$ ratios used for calculating the initial $^{143}Nd/^{144}Nd$ isotopic ratios obtained during the high-precision runs were determined using the SA ICP-MS technique. The precision and accuracy of determining the $^{147}Sm/^{144}Nd$ ratio was assessed by analyzing

multiple aliquots of the USGS GRM BCR-1 and BIR-1. The average values obtained during the course of this analytical campaign were 0.1397±8 (N = 4, 2SD) and 0.2798±24 (N = 18, 2SD) for BCR-1 and BIR-1, respectively (Puchtel *et al.*, 2016b). The average $^{147}Sm/^{144}Nd$ ratio for BCR-1 is identical, within the uncertainty, to the average $^{147}Sm/^{144}Nd$ = 0.13939±16 (N = 4, 2SD) obtained at the *IGL* using the ID-TIMS technique (Puchtel et al., 2013). The larger uncertainty on the $^{147}Sm/^{144}Nd$ ratio obtained for BIR-1 in this study (0.9%) compared to BCR-1 (0.5% relative) can be ascribed either to the apparently slightly larger sample powder heterogeneity of BIR-1 compared to BCR-1 (Puchtel *et al.*, 2016a) or lower REE abundances in BIR-1 compared to BCR-1. Since the REE concentration range in the BCF is more similar to REE abundances in BCR-1, we used the external reproducibility of the $^{147}Sm/^{144}Nd$ ratio obtained for BCR-1 as a measure of uncertainty on the $^{147}Sm/^{144}Nd$ obtained in this study (0.5%, 2SD).

The initial $\varepsilon^{143}Nd$ values were calculated based on the present-day parameters of the Chondritic Uniform Reservoir (CHUR): $^{147}Sm/^{144}Nd$ = 0.1967 (Jacobsen and Wasserburg, 1980), $^{143}Nd/^{144}Nd$ = 0.512638 (Hamilton et al., 1983).

3.6. Lu-Hf isotopic compositions and abundances

The Lu-Hf concentration and isotopic measurements were carried out at the Ecole Normale Supérieure de Lyon (*ENSL*), France. The sample dissolution procedure, employing Parr bombs and a mixed >98% pure ^{176}Lu-^{180}Hf spike, and the Lu and Hf separation protocols used are described in (Blichert-Toft *et al.*, 1997), (Blichert-Toft, 2001), and (Blichert-Toft and Puchtel, 2010). Lutetium and Hf isotopic compositions were measured by multi-collector ICP-MS using the *Nu Plasma 500 HR* coupled with a *DSN-100* desolvating nebulizer and following the protocols of (Blichert-Toft *et al.*, 1997; Blichert-Toft *et al.*, 2002). Hafnium was normalized for instrumental mass fractionation relative to $^{179}Hf/^{177}Hf$ = 0.7325 using an exponential law. The JMC-475 Hf standard was analyzed every two samples and gave, during the present single analytical session, an average $^{176}Hf/^{177}Hf$ = 0.282164±0.000010 (2SD; N = 8), which represents the estimate of the external precision of the Hf isotopic analyses (0.0035%). Since this value is identical, within uncertainty, to the accepted value for the JMC-475 Hf standard of 0.282163±0.000009 (Blichert-Toft and Albarède, 1997), no further corrections were applied to the data. We used the uncertainty obtained from the external reproducibility of the Hf standard as the uncertainty on the Hf isotopic composition for the isochron calculations, except for the two samples (BC08 and BC10; Table S7) for which the internal run precision was slightly larger than the external reproducibility, in which case the

in-run error was used. The uncertainty on the Lu/Hf ratio was 0.2% and this was the value we used for the isochron calculations for all samples. Total analytical blanks were <20 pg for both Lu and Hf.

For the isochron calculations, ISOPLOT 3.00 (Ludwig, 2003) and the ^{176}Lu decay constant of 1.867×10^{-11} $year^{-1}$ (Scherer et al., 2001; Söderlund et al., 2004) were used. The $\varepsilon^{176}Hf$ values were calculated as parts per 10,000 deviation of the measured sample $^{176}Hf/^{177}Hf$ at the time of komatiite lava emplacement from the chondritic reference defined as $^{176}Lu/^{177}Hf = 0.0336$ and $^{176}Hf/^{177}Hf = 0.282785$ (Bouvier et al., 2008).

4. Results

4.1. Major and lithophile trace element abundances

Major and trace element concentration data for the BCF are listed in Tables 3 and 4, and selected elements are plotted on variation diagrams in Fig. 2 and as BSE-normalized values in Fig. 3. The elemental abundances vary in the regular fashion typical of thick differentiated komatiitic basalt lava flows, such as the Fred's Flow in the AGB (Arndt, 1977). The MgO abundances range between 13.4 and 8.17 wt. % in the clinopyroxene-spinifex zone, increase to 28.5 wt. % in the uppermost part of the cumulate zone and reach a maximum of 34.0 wt. % about halfway down the cumulate zone. The rocks are characterized by high total Fe_2O_3 abundances of up to 19.3 wt. % in the spinifex zone and 22.2 wt. % in the cumulate zone (Table 3).

Most lithophile trace element abundances plot on well-defined trends with negative slopes in MgO versus trace element variation diagrams (Fig. 2). As is evident from Fig. 2, the BCF is significantly depleted in Al_2O_3 ($Al_2O_3/TiO_2 = 5.2\pm0.2$, 2SE) relative to the typical Al-undepleted komatiites from Munro Township. These correlations reflect mainly olivine, with subordinate clinopyroxene, control over the BCF compositional range. These trends further indicate immobile behavior of most elements of interest during secondary alteration processes.

The BSE-normalized lithophile trace element abundances are characterized by enrichments in light REE ($(La/Sm)_N$ = 1.88±0.05, 2SE) and depletions in heavy REE ($(Gd/Yb)_N$ = 2.02±0.05, 2SE); all samples exhibit small negative Zr and Hf anomalies (Fig. 3). Based on the coupled depletions in Al_2O_3 and heavy REE, the BCF lava belongs to the Al-depleted komatiite type of (Nesbitt *et al.*, 1979).

4.2. Re-Os isotopic compositions and HSE abundances

The Re-Os isotopic and HSE abundance data for the BCF are listed in Table 5 and plotted on a Re-Os isochron diagram in Fig. 4, on the CI chondrite-normalized spider diagram in Fig. 5, and on MgO versus HSE variation diagrams in Fig. 6. Thirteen samples (including replicates and excluding sample BC06, which plots well above the regression line), define a regression line with a slope corresponding to an ISOPLOT Model 3 age of 2728±23 Ma and a chondritic, albeit imprecise, initial $^{187}Os/^{188}Os$ = 0.1122±38 ($\gamma^{187}Os$ = +3.6±3.4). This age is in agreement with the U-Pb zircon age of 2720±2 Ma obtained by (Corfu and Noble, 1992) for the tholeiitic succession that hosts the BCF. The large uncertainty on the initial $\gamma^{187}Os$ value derived from the regression is due to scatter (MSWD = 140) of the data for samples with high $^{187}Re/^{188}Os$ ratios. Averaging the initial $^{187}Os/^{188}Os$ ratios for samples with $^{187}Re/^{188}Os < 0.5$, which also have the highest Os abundances, yields a more precise average initial $\gamma^{187}Os(T) = -0.58\pm0.90$ (2SD). This chondritic value is inconsistent with the subchondritic $\gamma^{187}Os$ value of −3.8±0.5 obtained by (Walker and Stone, 2001), even though the Re-Os ages obtained in the two studies are identical within their respective uncertainties (2708±13 and 2728±23 Ma).

The source of this discrepancy is not clear. Data for sample powders J17 and 2-18 analyzed in both studies show ~50% higher Re abundances in the study by (Walker and Stone, 2001); this resulted in 1.5-3.1% lower calculated initial $\gamma^{187}Os$ values for these samples compared to the present study (Table 5). One potential explanation is under-correction of the

475 total analytical blank for Re (17±5 pg compared to 0.34 pg in this study) given the very low
476 Re abundances in the cumulate samples. Additionally, from the *un-crushed material* of the
477 Walker and Stone (2001) study we prepared a new powder for sample J17 (labeled J17_1)
478 using metal-free equipment. This new sample powder has 46% lower Re abundance
479 compared to the powder for this sample from the Walker and Stone (2001) study that we also
480 analyzed here (Table 5). This may be due to minor Re contamination during sample
481 preparation in the Walker and Stone (2001) study because of the very low Re abundances in
482 these samples (0.048 ppb Re in the new sample powder J17_1). Correction of the 46% surplus
483 Re brings the calculated initial γ^{187}Os value for sample powder J17 up to an average of +0.11
484 (based on our two replicate analyses), which is similar to the average initial γ^{187}Os value of
485 +0.50 obtained on two replicate analyses of the new powder for this sample, J17_1.
486 Due to the lack of un-crushed material for sample 2-18, we were unable to evaluate the
487 degree of Re contamination (if any) of this sample; as a result, we used uncorrected γ^{187}Os
488 values for this sample in calculating the average initial γ^{187}Os. When re-calculating the
489 average initial γ^{187}Os for the low-^{187}Re/^{188}Os samples and including the contamination-
490 corrected γ^{187}Os for sample J17, a precise average initial γ^{187}Os = +0.06±0.34 is obtained.
491 This value is our best estimate of the initial ^{187}Os/^{188}Os isotopic composition of the BCF
492 mantle source.
493 In the CI chondrite-normalized diagrams (Fig. 5) and MgO versus HSE variation
494 diagrams (Fig. 6), Os, Ir, and Ru abundances increase in the samples from the cumulate zone
495 compared to those from the spinifex zone; however, Os and Ir, and to a lesser extent Ru,
496 abundances also show large (*e.g.,* Os = 0.16–3.0 ppb) variations within the samples from the
497 cumulate zone itself, which are independent of the MgO content in these samples. This type
498 of variation is typical of the so-called Munro-type lavas (Puchtel and Humayun, 2005), where

abundances of these elements are controlled mostly by fractionation of Os-Ir alloy during lava differentiation upon emplacement.

Platinum and Pd abundances exhibit strong negative correlations with MgO contents and decrease from spinifex to cumulate zone of the BCF (Fig. 5); the data plot on the trends that intersect the MgO axes at 53±2 and 48±1 wt. % MgO, respectively (Fig. 6). While the trend for Pd is consistent with olivine control, the trend for Pt is somewhat shallower, indicating presence on the liquidus of a phase in addition to olivine that affected to some extent variations of Pt during differentiation of the BCF.

Finally, Re abundances in the spinifex-textured samples plot with significant scatter (Fig. 6). This likely indicates Re mobility during alteration of the BCF, including gain/loss of Re in the spinifex-textured samples and net loss in the cumulate samples. The observed Re mobility evidently took place shortly after emplacement of the BCF, with the Re-Os system remaining undisturbed since then, as evidenced by the correct Re-Os isochron age obtained.

4.3. W isotopic compositions and abundances

Tungsten abundances and isotopic compositions are listed in Table 6 and plotted in Figs. 2-3 and 7. The W abundances vary from 245 to 1305 ppb. The highest W abundance (1305 ppb) is observed in sample powder J17 from the Walker and Stone (2001) study. In the new sample powder J17_1 that was prepared for this study from un-crushed material of sample J17 using metal-free equipment, the W concentration is ~4× lower (347 ppb). This is consistent with the ~50% higher Re abundance in sample J17 compared to J17_1 and supports the conclusion that sample J17 was contaminated with metal during sample preparation in the Walker and Stone (2001) study. Sample 2-18, which has a ~2× higher W abundance compared to sample J17_1, was also likely contaminated with W (and possibly Re) during sample preparation in the Walker and Stone (2001) study, although to a lesser degree than

sample J17. As such, W abundance data for samples J17 and 2-18 were excluded from further discussion and no W isotopic data were obtained for these samples for the same reason.

In the MgO versus trace element diagrams (Fig. 2), W abundances plot with significant scatter around a trend with a slightly positive slope. The BSE-normalized trace element abundances (Fig. 3) are characterized by variable positive W anomalies relative to neighbouring elements (*i.e.*, Th and U) with similar incompatibility during mantle melting (W/W* = 1.6–13, where $W/W^* = W_N/(\sqrt{[Th_N \times U_N]})$, and *N* are BSE normalized values from (Arevalo and McDonough, 2008) and (Hofmann, 1988). In the upper part of the spinifex zone, the W/W* ratio varies between 1.6 and 2.4, indicating presence of only a small positive W abundance anomaly. Across the BCF, W abundances increase in the cumulate zone relative to the spinifex zone, displaying a positive correlation with MgO contents (Fig. 2). There is also a positive correlation between W/W* and LOI values (Fig. 3b).

All the BCF samples analyzed are characterized by $^{182}W/^{184}W$ ratios higher than the $^{182}W/^{184}W$ measured in the terrestrial standard, with an average $\mu^{182}W$ value of +11.7±4.5 (2SD, $n = 12$), where $\mu^{182}W$ is the parts per million deviation of $^{182}W/^{184}W$ of a given sample from that of the terrestrial standard, which, by definition, is equal to zero (Table 6, Fig. 7).

4.4. Sm-Nd and Lu-Hf isotopic compositions and abundances

The Sm-Nd isotopic data for the BCF are listed in Table 7 and plotted in Figs. 8 and 9. All samples analyzed are characterized by small ^{142}Nd deficits, with an average $\mu^{142}Nd = -3.8\pm2.8$ (2SD, $n = 15$), where $\mu^{142}Nd$ is the parts per million deviation of $^{142}Nd/^{144}Nd$ of a given sample from that of the terrestrial standard, which, by definition, is equal to zero (Table 7, Fig. 8). The average $^{142}Nd/^{144}Nd$ of the BCF, however, is not resolvable, within the uncertainty, from that of the terrestrial Nd standard AMES analyzed during the course of this analytical campaign ($\mu^{142}Nd = 0.0\pm2.8$, 2SD; $N = 34$).

547 The ^{147}Sm-^{143}Nd data (Fig. 9a) for the BCF yield a Model 1 ISOPLOT isochron age of
548 2719±170 Ma (MSWD = 0.89), which is identical to the U-Pb emplacement age of 2720±2
549 Ma. This indicates that the samples from the BCF behaved as closed systems with regard to
550 their Sm–Nd isotope systematics. This conclusion is also supported by the magmatic nature of
551 the variations of the Sm and Nd abundances in the samples across the BCF as a function of
552 their MgO contents (Fig. 2). Due to the limited variation in the Sm/Nd ratio among the
553 samples, the ISOPLOT regression analysis produced a rather imprecise isochron age and an
554 initial $\varepsilon^{143}Nd$ = +2.6±3.0, where $\varepsilon^{143}Nd$ is the parts per ten thousand deviation of the
555 $^{143}Nd/^{144}Nd$ ratio of a given sample from the chondritic, or BSE, reference value. A more
556 precise initial $\varepsilon^{143}Nd$ = +2.5±0.2 (2SD, *n* = 15) is obtained by averaging the initial
557 $^{143}Nd/^{144}Nd$ ratios calculated for each sample using the measured $^{147}Sm/^{144}Nd$ and
558 $^{143}Nd/^{144}Nd$ ratios and the BCF emplacement age of 2720 Ma.
559 The ^{176}Lu-^{176}Hf data (Fig. 9b) for the BCF define a correlation in $^{176}Lu/^{177}Hf$ – $^{176}Hf/^{177}Hf$
560 space corresponding to a Model 3 ISOPLOT age of 2489±880 Ma (MSWD = 5.4), which also
561 overlaps, within the uncertainties, the U-Pb emplacement age of the BCF. As with the Sm-Nd
562 isotopic system, the limited range in the Lu/Hf ratios among the samples precludes
563 determination of more precise age and initial $\varepsilon^{176}Hf$, defined as the parts per ten thousand
564 deviation of the $^{176}Hf/^{177}Hf$ ratio of a given sample from the chondritic reference value (Table
565 8, Fig. 9b). Averaging initial $\varepsilon^{176}Hf$ values of individual samples calculated using the
566 measured $^{176}Lu/^{177}Hf$ and $^{176}Hf/^{177}Hf$ ratios and the BCF emplacement age of 2720 Ma yields
567 a more precise average initial $\varepsilon^{176}Hf$ = +4.2±0.9 (2SD, *n* = 6).
568 Similar to other late Archean and post-Archean komatiite and basalt systems, the
569 calculated initial $\varepsilon^{143}Nd$ and $\varepsilon^{176}Hf$ ratios of the BCF plot on the terrestrial array of (Blichert-
570 Toft and Puchtel, 2010), indicating coupled, or congruent, normal depleted mantle behavior of
571 the Nd-Hf isotope systems in the mantle source of the BCF (Fig. 9c).

5. Discussion

5.1. Komatiite or picrite?

There is some controversy in the literature regarding the composition of the parental magma (komatiitic or picritic) and the source of the BCF. In their original study, (Stone *et al.*, 1987) emphasized that the BCF exhibited the two most important features of komatiitic rocks: spinifex-texture and the crystallization sequence Ol − Cpx − Pl. Based on the geochemical similarity of the BCF to the Al-depleted komatiites from the Barberton GB and the textural and petrographic features typical of komatiites, these authors concluded that the BCF was an example of a thick, layered, Al-depleted komatiite that may have been derived from an Fe- and Ti-enriched lower mantle following development of a chemically layered mantle during the Archean. (Walker and Stone, 2001) referred to the BCF as an Fe-enriched komatiite flow. These authors concluded that the parental melt to the BCF was either derived from early Archean, melt-depleted subcontinental lithospheric mantle (based on the strongly subchondritic initial $^{187}Os/^{188}Os$ isotopic composition that has not been confirmed in this study), or was sourced from a portion of the mantle that retained some characteristics of early Earth formation, such as majorite fractionation from a primordial magma ocean.

In the recent compilation by (Arndt *et al.*, 2008), the BCF was referred to as komatiite and was argued to be similar to the other Fe- and Ti-enriched, Al-depleted komatiites, *e.g.*, from the 3.0 Ga Meekatharra–Wydgee GB of the Yilgarn Block in Western Australia (Barley *et al.*, 2000), the 2.93 Ga Steep Rock and Lumby Lake GB in the Northern Superior Province, Canada (Hollings and Wyman, 1999; Tomlinson *et al.*, 1999), the 2.70 Ga Vermillion GB of Minnesota (Green and Shulz, 1977; Schulz, 1982), the 2.11 Ga Inini GB of the Guiana shield (Capdevila *et al.*, 1999), and the 2.06 Ga Lapland-Karasjok GB (Barnes and Often, 1990; Hanski *et al.*, 2001). Due to the rather wide distribution and specific geochemical features of

these lavas, (Barley *et al.*, 2000) coined the term Karasjok-type komatiites after the locality in Norway, where they were first described by (Barnes and Often, 1990).

The majority of models that explain the origin of the Karasjok-type komatiites (Capdevila *et al.*, 1999; Tomlinson *et al.*, 1999; Barley *et al.*, 2000) involve deep, high-degree anhydrous melting in mantle plumes in equilibrium with residual majorite garnet, typical of the Al-depleted komatiites (Ohtani, 1984; Herzberg and Ohtani, 1988; Ohtani, 1990). This model is consistent with the estimates of the pressure of melting for the BCF to be between 10 and 14 GPa (Herzberg and O'Hara, 2002), which is similar to that for the Barberton komatiites. In order to explain the variable enrichments in Fe and Ti of the Karasjok-type komatiites, (Hanski *et al.*, 2001) proposed that they were derived from a mantle plume source that was heterogeneous, likely because it contained variable, but small amounts of recycled eclogite.

(Arndt, 1994) pointed out that the crucial feature that distinguishes komatiites from picrites is the presence of spinifex texture in the former. This feature owes its origin to the early history of komatiite magmas as superheated liquids that picritic magmas are lacking altogether, which, in turn, stems from the extremely high temperature as the defining feature of the komatiite source. (Donaldson, 1979) and (Lofgren, 1983) have shown experimentally that a period of superheating strongly influences the subsequent crystallization history of a silicate liquid. The process of heating a silicate melt well above its liquidus breaks down the structure of the liquid, destroying the chains and networks that act as nuclei during crystallization on subsequent cooling. A liquid subjected to superheating crystallizes quite differently from one that was never superheated. Superheated liquids display a reluctance to nucleate when cooled and the crystals that do form tend to be few, large and skeletal. Komatiite magma follows a path through the mantle that takes it to temperatures well above the liquidus. The period of superheating has the effect that nucleation is inhibited, relatively

few phenocrysts form, and heterogeneous nucleation on quenched margins is favored; spinifex texture is the consequence.

Contrary to their earlier study, (Stone *et al.*, 1995a), while acknowledging the close spatial and temporal association of the BCF with komatiites from the Abitibi greenstone belt, likely indicating their origin in a hot mantle, proposed that the parental magma that gave rise to the BCF was a ferropicrite with <18% MgO. According to these authors, the geochemistry of the BCF can be explained by a two-source-component mixing model. The first source component was peridotite depleted by extraction of melt prior to generation of the BCF magma, whereas the second one was highly enriched small-degree melt fractions formed in the majorite stability field in the mantle. Mixing of the two source components was proposed to have occurred immediately prior to melting to maintain the radiogenic Nd isotopic composition.

In this study, we consider the BCF to be komatiitic in origin based on their textural and chemical features and close spatial and temporal association with the Al-undepleted (Munro Township: (Arndt *et al.*, 1977; Arndt and Nesbitt, 1984; Arndt, 1986) and Al-depleted (Newton Township: (Cattell and Arndt, 1987) komatiites. Following the conventional model for the origin of the Karasjok-type komatiites (Capdevila *et al.*, 1999; Tomlinson *et al.*, 1999; Barley *et al.*, 2000), we consider the parental magma to the BCF to be a product of relatively high-degree partial melting of a melt-depleted, but Fe- and Ti-enriched source. Melting started deep (300-420 km) in the mantle in the majorite stability field based on the estimates of (Herzberg and O'Hara, 2002), which resulted in the strong Al-depleted signature of the parental melt. According to (Herzberg, 1992), Al-depleted komatiitic parental melts that formed under such conditions were derived by high degrees (~50%) of pseudo-invariant melting (L + Ol + Gt + Cpx) of fertile mantle peridotite in the 80- to 100-kbar range, about 260- to 330- km depth. The enrichment in incompatible lithophile trace elements could have resulted from mixing of the parental komatiitic magma with low-degree partial melts derived

from the same heterogeneous plume; this type of magma mixing and enrichment has been previously advocated for komatiites from Munro and Newton Townships, Ontario (Arndt and Nesbitt, 1984; Cattell and Arndt, 1987). Following this train of logic, we also assume that the parental magma to the BCF had a MgO content similar to the other Al-depleted komatiites in the area, *i.e.*, it contained 25-27 wt. % MgO (Cattell and Arndt, 1987); this parental magma fractionated olivine *en route* to the surface to reach ~16 wt. % MgO upon emplacement.

5.2. HSE systematics of the Boston Creek Flow mantle source

The absolute and relative abundances of HSE in the mantle bear on such key topics as core-mantle differentiation, late-stage planetary accretion and subsequent core-mantle exchange. Here, we use the initial $^{187}Os/^{188}Os$ ratio obtained for the BCF to calculate the time-integrated Re/Os in its mantle source by assuming generation of this mantle source soon after Solar System formation. It is estimated, therefore, that this source would have evolved from the Solar System initial $^{187}Os/^{188}Os = 0.0952\pm2$ at 4568 Ma (Day *et al.*, 2016) to the initial $^{187}Os/^{188}Os = 0.10846\pm36$ at 2720 Ma with a time-integrated $^{187}Re/^{188}Os = 0.404\pm11$. This ratio is well within the range observed for chondritic meteorites (average $^{187}Re/^{188}Os = 0.410\pm51$ (2SD), as compiled from the data of (Walker *et al.*, 2002; Brandon *et al.*, 2005; Fischer-Gödde *et al.*, 2010). The calculated initial $^{187}Os/^{188}Os$ of the BCF source is also well within the range of those for the majority of Archean komatiite systems, as evidenced by a compilation of $^{187}Os/^{188}Os$ isotopic data for Archean komatiites (Fig. 10).

As has been discussed previously (Puchtel *et al.*, 2016b), more than 90% of the HSE budget of the mantle resides in two types of sulfides (Alard *et al.*, 2000; Lorand and Alard, 2001; Luguet *et al.*, 2007). The high-temperature Os-Ir-Ru-rich Fe-Ni monosulfide solid solution (*mss*) forms rounded inclusions in olivine, whereas low-temperature, irregular-shaped Cu-Ni sulfides occupy intergranular space. During partial melting of mantle peridotite, Cu-Ni sulfides enter the melt, whereas the *mss* remains trapped in the melting residue until the

degree of melting reaches 20-25% (Barnes *et al.*, 1985; Keays, 1995; Luguet *et al.*, 2007; Fonseca *et al.*, 2011; Fonseca *et al.*, 2012), at which point all the low-temperature sulfide in the residue gets consumed and, as the degree of melting continues to increase, the magma becomes sulfide-undersaturated. It has also recently been shown that decrease in fS_2 with increase in degree of melting triggers exsolution of Os-Ir alloys from the refractory *mss* in the residue (Fonseca *et al.*, 2011; Fonseca *et al.*, 2012). All low-degree (basalts) and the majority of higher-degree (picrites and komatiites) partial melts are charactrized by compatible behavior of Os and Ir during magmatic differentiation, indicating that their parental magmas remained saturated in Os-Ir alloys (Puchtel *et al.*, 2004b; Barnes and Fiorentini, 2008). However, some lavas, such as the 2.8 Ga Kostomuksha and the 3.55 Ga Schapenburg komatiites, exhibit incompatible behavior of Os and Ir during magma differentiation, likely indicating near-complete exhaustion of Os-Ir alloys in the mantle sources of these komatiites (Puchtel and Humayun, 2005; Puchtel *et al.*, 2009a).

In order to calculate the absolute HSE abundances in the mantle source of the BCF, the projection technique of (Puchtel *et al.*, 2004b), subsequently modified by (Puchtel *et al.*, 2016b) to be applicable to komatiitic lavas derived from parental magmas that experienced fractional crystallization *en route* to the surface, and the HSE abundances in the BCF obtained in this study, were used. Due to the poorly constrained differentiation history of the BCF magma prior to emplacement in terms of Os, Ir, and Ru fractionation, and mobile post-emplacement behavior of Re, only abundances of the incompatible and immobile elements Pt and Pd in the BCF source could be estimated with a sufficiently high degree of accuracy.

One of the pre-requisites for this protocol to be applicable is the complete exhaustion of low-temperature sulfides harboring Pt and Pd in the mantle source during partial melting. Based to the models of magma generation for Karasjok-type komatiites (Capdevila *et al.*, 1999; Tomlinson *et al.*, 1999; Barley *et al.*, 2000) and following estimates of (Herzberg and

O'Hara, 2002) for the depth of the BCF magma generation (300-420 km), in equilibrium with residual majorite garnet, the BCF parental magma was estimated to have formed via moderate to high degrees (>25%) of partial melting of an already melt-depleted source in a mantle plume and, therefore, must have been sulfide undersaturated prior to emplacement. According to (Herzberg, 1992), Al-depleted komatiitic parental melts that form under such conditions were derived by high degrees (~50%) of pseudo-invariant melting (L + Ol + Gt + Cpx) of fertile mantle peridotite in the 80- to 100-kbar range, about 260- to 330- km depth; as such, the 25% degree partial melting is likely the minimum estimate. The strongest evidence for the sulfide-undersaturated nature of the BCF is provided by the incompatible behavior of Pd during differentiation. Palladium abundances across the BCF plot on an olivine control line in MgO–Pd space (Fig. 6), indicating that sulfide liquid was not a fractionating phase within the compositional range represented by the samples of this study.

It should be noted, however, that the sulfur content at saturation of a mafic magma increases with decreasing pressure, so magmas may become undersaturated during adiabatic ascent (Mavrogenes and O'Neill, 1999). This limitation can only be relaxed if there are no sulfides left in the source after melt separates from the residue, which can only be attained if the degree of melting exceeds ~20-25%, as discussed earlier (Fonseca *et al.*, 2011; Fonseca *et al.*, 2012). This degree of melting is lower than estimated for the formation of the BCF parental melt. In addition, at temperatures and pressures of komatiite formation, sulfur becomes even more soluble, and komatiite sources become S-undersaturated at even lower degrees of partial melting (Barnes and Fiorentini, 2008).

The first step in calculating the Pt and Pd abundances in the BCF mantle source is to establish the original liquid lines of descent for this komatiitic basalt system. For incompatible Pt and Pd, these liquid lines of descent should pass through the composition of the liquidus olivine that was in equilibrium with the parental komatiite magma with ~27 wt. % MgO, and

720 the composition of the BCF emplaced lava, which resulted from fractionation of this liquidus
721 olivine from the parental komatiite magma. For the present calculations, the Pt and Pd
722 abundances and MgO content of the Pyke Hill komatiitic olivine from (Puchtel *et al.*, 2009b)
723 were used. This choice was based on the assumption that a komatiitic magma similar in MgO
724 content to that at Pyke Hill most likely was the parental magma to the BCF (see the
725 discussion above). Besides, since both Pt and Pd are highly incompatible in olivine (*e.g.,*
726 (Brenan *et al.*, 2003), small variations in the abundances of these elements in the olivine
727 would have had negligible effect on the calculated Pt and Pd abundances in the BCF mantle
728 source. Using the above assumptions and ISOPLOT regression analysis to project the
729 abundances of Pt and Pd measured in the spinifex-textured samples of the BCF in this study
730 and in the Pyke Hill olivine from (Puchtel *et al.*, 2004b), to mantle MgO = 38 wt. %., the Pt
731 and Pd abundances in the BCF source were calculated to be 2.4±0.2 and 2.8±0.3 ppb,
732 respectively (2SD, propagated error). From these results, the total Pt and Pd abundances in the
733 BCF source were calculated to be 5.2±0.7 ppb, or 35±5% of those in the estimates for modern
734 BSE of 14.7±2.0 ppb (Becker *et al.*, 2006).
735 The calculated total Pt and Pd abundances in the source of the BCF are plotted as a
736 function of age and compared with those in the sources of other Archean komatiite systems
737 and the BSE (Fig. 11). The calculated total Pt and Pd abundances in the source of the BCF are
738 substantially lower than those in any of the late Archean komatiite systems studied to-date,
739 which range from 57±4% in the 2.69 Ga Belingwe to 86±6% in the 2.72 Ga Alexo systems,
740 relative to those in the estimates for modern BSE. The only komatiite system with lower total
741 Pt and Pd abundances is 3.55 Ga Schapenburg with 29±5%.

742 ***5.2. Origin of the positive ^{182}W anomaly***

743 The first issue to address before discussing the significance of the positive ^{182}W anomaly
744 is the origin of W in the BCF and whether or not it is representative of its mantle source. On a

745 BSE-normalized plot (Fig. 3), W abundances are characterized by variable positive offsets,
746 relative to Th and U, the lithophile trace elements with similar incompatibility during mantle
747 melting under redox conditions close to the FMQ buffer (König *et al.*, 2011). Further, W
748 abundances plot on a trend versus MgO that is oblique to the olivine control line (Fig. 2). This
749 most likely indicates W disturbance during seafloor alteration and/or metamorphism. This
750 conclusion is further confirmed by the positive correlation between indices of alteration, *i.e.*,
751 loss on ignition (LOI), and W/W*, *i.e.*, the magnitude of the W abundance offset relative to U
752 and Th (Fig. 3b). At the same time, there is a negative correlation between indices of
753 alteration and the magnitude of the positive ^{182}W anomaly (Fig. 3c). Moreover, all samples
754 collected across the BCF show uniformly positive ^{182}W anomalies. These observations
755 suggest that the BCF itself was the source of W in the samples analyzed. It should be noted,
756 however, that no negative W/W* abundance anomalies have been found in any samples
757 analyzed that would counter-balance the positive W/W* abundance anomalies in the others.
758 This could indicate that the BCF parental melt has originally been enriched in W. Recently,
759 (Babechuk *et al.*, 2010) have found that many of the highly depleted mantle peridotites
760 contain far higher W concentrations than expected based on the abundances of similarly
761 incompatible lithophile trace elements, such as Th and U. In the absence of convincing
762 indications for alteration, re-enrichment or contamination, these authors concluded that the W
763 excess was caused by retention of W in an Os–Ir alloy phase. During high- degree partial
764 melting involved in komatiite formation, a significant proportion of the Os-Ir alloy that was
765 retained in the mantle source during extraction of low-degree melts would have entered the
766 komatiite melt, resulting in its enrichment in W relative to Th and U. This would be consistent
767 with the enrichment in W in the cumulate zone of the BCF that is also enriched in Os and Ir
768 relative to the spinifex zone. As such, we conclude that the W isotopic composition obtained
769 for the BCF can be considered to be that of the mantle source of the BCF.

770 The ^{182}Hf-^{182}W isotopic system ($t_{½}$ = 8.9 Ma) has been commonly used in
771 cosmochemistry to constrain the timing of metal-silicate segregation (Kleine *et al.*, 2002;
772 Kleine *et al.*, 2004a; Kleine *et al.*, 2004b; Touboul *et al.*, 2007; Kleine *et al.*, 2009; Touboul
773 *et al.*, 2015). This is due to the fact that Hf is strongly lithophile, while W is moderately
774 siderophile, and both elements are highly refractory. Thus, Hf is fractionated from W during
775 metal-silicate differentiation, such as that occurring during planetary core segregation. In
776 addition to cosmochemical applications, studies of terrestrial rocks spanning the history of
777 Earth's rock record have documented both positive and negative ^{182}W anomalies (Willbold *et*
778 *al.*, 2011; Touboul *et al.*, 2012; Touboul *et al.*, 2014; Willbold *et al.*, 2015; Puchtel *et al.*,
779 2016a; Puchtel *et al.*, 2016b; Rizo *et al.*, 2016a; Rizo *et al.*, 2016b; Dale *et al.*, 2017; Mundl
780 *et al.*, 2017). These isotopic anomalies have been interpreted within the framework of three
781 broad categories of processes.
782 The first category is core-mantle interaction. Assuming chondritic ^{182}W/^{184}W for bulk
783 Earth (*i.e.,* $\mu^{182}W = -190\pm10$: (Kleine *et al.*, 2002; Schoenberg *et al.*, 2002; Yin *et al.*, 2002;
784 Kleine *et al.*, 2004a), 13 ppb W for BSE (Arevalo and McDonough, 2008; König *et al.*, 2011)
785 and 590 ppb W for the core (McDonough, 2004), mass balance calculations require the core
786 to have a $\mu^{182}W$ of ~ −220 to balance the more radiogenic isotopic composition of the BSE
787 ($\mu^{182}W = 0$). Addition of core metal to a mantle domain would, therefore, lead to a decrease in
788 the $\mu^{182}W$ value of that mantle domain.
789 The second category capable of generating ^{182}W heterogeneity in the mantle is metal-
790 silicate or silicate-silicate fractionation processes that operated within the first ~50 Ma of
791 Solar System history, while ^{182}Hf was still extant (*e.g.,* (Touboul *et al.*, 2012). Metal-silicate
792 fractionation, followed by removal of the metal from an isolated mantle domain, such as a
793 basal magma ocean, would leave the silicate domain with suprachondritic Hf/W, due to
794 preferential partitioning of W into the metal. Alternatively, crystal-liquid fractionation in a

795 purely silicate system, such as a global magma ocean, would lead to high Hf/W in early
796 formed cumulates and low Hf/W in the residual liquid, due to the more incompatible nature of
797 W compared with Hf. If any of these fractionation processes occurred while ^{182}Hf was still
798 extant, excesses in ^{182}W would eventually be created in both the silicates left after metal
799 segregation and the silicate cumulates in the differentiated primordial magma ocean. By
800 contrast, a complementary residual magma ocean liquid would develop deficits in ^{182}W,
801 compared to the ambient mantle.
802 The third category is disproportional late accretion (Willbold *et al.*, 2011; Kruijer *et al.*,
803 2015; Touboul *et al.*, 2015; Willbold *et al.*, 2015). Late accretion is a process commonly
804 proposed to account for high absolute, and chondritic relative abundances of HSE in the
805 modern mantle (Kimura *et al.*, 1974; Morgan *et al.*, 1981; Chou *et al.*, 1983). It requires
806 addition to the mantle of ~0.5 wt. % of Earth's mass (Walker, 2009) of HSE-rich
807 planetesimals with chondritic bulk compositions after last equilibration between the core and
808 mantle. Chondrites have ~20 times higher W abundances and −190±10 ppm less radiogenic
809 ^{182}W/^{184}W than the modern terrestrial mantle (Kleine *et al.*, 2002; Schoenberg *et al.*, 2002;
810 Yin *et al.*, 2002; Kleine *et al.*, 2004a); as a result, late accretion likely led to a decrease in the
811 ^{182}W/^{184}W ratio of the mantle by ~25 ppm compared to the pre-late accretionary mantle. The
812 fact that the ^{182}W/^{184}W of the HSE-poor lunar mantle is ~ 25 ppm higher than BSE provides
813 supporting evidence for this process (Kruijer *et al.*, 2015; Touboul *et al.*, 2015). Thus, any
814 mantle domain to which less of a late accretionary component was added, would be ^{182}W-
815 enriched, compared to the mantle to which a full complement of late accretionary component
816 was added. Such a mantle domain would also be expected to be depleted in HSE, compared to
817 BSE.
818 The positive ^{182}W anomaly observed in the BCF cannot be the result of core-mantle
819 interaction, as this process would decrease, rather than increase, ^{182}W/^{184}W in the mantle

source of the BCF. In addition, core-mantle interaction would have increased the HSE abundances in the BCF source over ambient mantle levels, whereas the BCF mantle domain is estimated to contain only ~35% of the total HSE complement of the BSE.

Crystal-liquid fractionation in a global magma ocean could have created cumulate-rich mantle domains with high Hf/W ratios that over a short period of time would have grown in excesses of ^{182}W; i.e., led to a positive $\mu^{182}W$ anomaly, just as observed in the BCF. However, early crystal-liquid fractionation would also have resulted in fractionation of the Sm/Nd ratio and, as a result, the creation of a positive ^{142}Nd anomaly complementary to the positive ^{182}W anomaly in the early magma ocean cumulates. Such an anomaly is not observed. In addition, unlike early Archean komatiite systems, the generation of which have been evoked to involve early magma ocean processes, partly owing to decoupled, or incongruent, Nd-Hf isotope systematics (Puchtel *et al.*, 2013; Puchtel *et al.*, 2016a), the BCF lavas plot on the terrestrial Nd-Hf array, suggesting minimal involvement of early magma ocean processes in the fractionation of the lithophile trace elements in the BCF mantle source (Fig. 8).

Metal-silicate fractionation, followed by removal of the metal from a basal magma ocean, would have fractionated the Hf/W ratio, and would have had no collateral effect on the Sm/Nd ratio and, therefore, neither on the ^{146}Sm-^{142}Nd systematics. Moreover, subsequent removal of the metal from the basal magma ocean would have driven the HSE abundances in the source of the BCF in the observed direction, i.e., towards the sub-BSE levels. This process would be equivalent in its net effect to the core formation event that occurred within the first 30 Ma of Solar System history (*e.g.,* (Yin *et al.*, 2002) and that have quantitatively stripped the mantle of HSE. However, this process would also have fractionated the Re/Os ratio in the mantle domain, that gave rise to the BCF, away from the chondritic value (*e.g.,* (Touboul *et al.*, 2012), which is not observed.

We conclude, therefore, that disproportional late accretion is the best explanation for the observed positive ^{182}W anomaly in the BCF. If late accreted materials were not rapidly mixed and homogenized throughout the mantle, as seems likely to have been the case in the context of the so-called stochastic late accretion (Bottke et al., 2010), where late accreted material consisted of a few large (up to 3,000 km in diameter) planetesimals, then portions of the mantle would be expected to initially have both excesses and deficits of late accreted materials, compared to the average amount required to accommodate the HSE budget of the BSE (*e.g.,* (Willbold *et al.*, 2011; Willbold *et al.*, 2015).

In order to evaluate the effect of disproportional late accretion on the ^{182}W and HSE systematics, we plotted the $\mu^{182}W$ in the BCF versus the total calculated Pt and Pd abundances in its mantle source relative to those in the present-day BSE (Fig. 12). This proportion corresponds to the fraction of the total HSE budget of the BSE added during late accretion assuming an HSE-free mantle following core formation. The W isotopic composition of the BSE prior to late accretion is constrained by the $^{182}W/^{184}W$ data for the lunar mantle to be +25±5 ppm (Kruijer *et al.*, 2015; Touboul *et al.*, 2015; Kruijer and Kleine, 2017). Our calculations indicate that, when the full uncertainties on the W isotopic composition of the BCF source and the pre-late accretion mantle are considered, the observed 11.5±4.5 ppm enrichment in ^{182}W would be achieved in a mantle domain to which 48±28% of late accreted materials, with chondritic W isotopic compositions, were added, relative to the present-day BSE. This is consistent with the calculated total HSE abundances in the source of the BCF of 35±5% of those in the estimates for the present-day BSE. At the same time, addition of even full complement of late accreted chondritic material with similar Nd abundance and negative $\mu^{142}Nd$ to the mantle will have negligible effect on both the Nd budget of the mantle and its Nd isotopic composition. We conclude, therefore, that stochastic late accretion, with incomplete mixing between mantle domains enriched and not enriched in

late accreted components, is the most plausible mechanism for the formation of the observed short- and long-lived isotopic and elemental systematics in the mantle domain that gave rise to the BCF. This mantle domain must have remained isolated from the rest of the convecting mantle at least until the formation of the BCF at 2.72 Ga, implying a long time scale for mixing of the terrestrial mantle, on the order of at least 1.8 billion years.

The predominant giant impact model of lunar formation requires the Moon to consist mainly of the material of the impactor (e.g., (Canup and Asphaug, 2001; Canup, 2004), which poses significant problems for this model in light of similarities of O, Si, and Ti isotopic compositions of the two planetary bodies (e.g., (Dauphas *et al.*, 2014). More recent dynamic models (e.g., (Canup, 2012), however, are more permissible of the formation of the Moon from the material of the Earth's mantle. This controversy can be addressed using the data of the present study. It can be expected that, if the ^{182}W excess in the BCF is attributed to the deficit of late accreted component in its mantle source alone, and if the ^{182}W composition of the lunar mantle largely corresponds to the ^{182}W composition of pre-late accretion BSE, the present day BSE, lunar mantle and the BCF source would plot on the single trend line in Figure 12. To test this hypothesis, we have performed ISOPLOT regression analysis using ±4.5 ppm as the uncertainty on both modern BSE and BCF source ^{182}W compositions and ±5% (absolute) as an uncertainty on the modern BSE and BCF source total HSE abundances. The results of the regression analysis indicate that the calculated pre-late accretion BSE had an ^{182}W excess of 18±7 ppm. This result is identical to the independently estimated ^{182}W isotopic composition of the BSE of 18±9 by (Kleine and Walker, 2017). It is also identical to the estimates for the ^{182}W composition of the Moon of +25±5 ppm, thus, providing further support to the notion that the Moon and Earth formed from material with identical ^{182}W compositions (Kleine and Walker, 2017).

5.3. Mechanisms of isolation of late accreted materials in the mantle

It is estimated, based on the studies of HSE abundances and Re-Os isotope systematics in terrestrial mantle samples (Meisel *et al.*, 2001; Becker *et al.*, 2006; Fischer-Gödde *et al.*, 2011) and derivative mantle melts from the martian (Brandon *et al.*, 2012) and lunar (Warren *et al.*, 1989; Ringwood, 1992; Righter *et al.*, 2000; Walker *et al.*, 2004; Day *et al.*, 2007; Day and Walker, 2015) mantles that the mass ratio of late accreted materials for the three bodies was ~1:10:1200. However, the Earth/Moon impact number flux ratio for both late accreted planetesimals and present-day near-Earth objects is ~20, with this value being a reflection of different gravitational cross sectional areas of the two bodies (Bottke *et al.*, 2007). It was concluded, therefore, to be highly unlikely that numerous, small projectiles could have achieved an Earth/Moon mass influx ratio close to 1200, especially in the aftermath of the Moon-forming event, when most leftover planetesimals and asteroids in the inner Solar System were dynamically excited (Bottke *et al.*, 2002; Bottke *et al.*, 2007).

It is also likely that most HSE were delivered to the terrestrial, martian, and lunar mantles within ~200 Ma of core formation termination on Earth. This is due to the fact that the lunar crust, which formed between 4.34 and 4.37 Ga (Borg *et al.*, 2014), is essentially intact and has only been modestly contaminated by extra-lunar materials (*e.g.*, (Morgan *et al.*, 1977; Norman *et al.*, 2002; Warren, 2003; Norman, 2005; Puchtel *et al.*, 2008; Fischer-Gödde and Becker, 2012). It has also been argued, based on the ^{142}Nd, ^{182}W, Re-Pt-Os, and HSE abundance data, that the 3.26-3.55 Ga Barberton komatiites (Puchtel *et al.*, 2014; Puchtel *et al.*, 2016a), 3.6-3.8 Inukjuak supracrustal rocks (Caro *et al.*, 2017), 3.8-4.3 Ga Isua supracrustal belt and the Nuvvuagittuq greenstone belt rocks (O'Neil *et al.*, 2016), as well as the 2.82 Ga Kostomuksha komatiites (Touboul *et al.*, 2012), were derived from mantle domains that were isolated from the rest of the mantle prior to ~4.40 Ga. On Mars, magma ocean crystallization and crust formation most likely occurred within 40 Ma of the Solar System history based on the combined ^{182}W–^{142}Nd systematics of a comprehensive suite of

martian meteorites (Kruijer *et al.*, 2017). This implies that most HSEs were delivered by leftover debris from terrestrial planet accretion, which was probably dominated by stony and/or differentiated planetesimals (Becker *et al.*, 2006). These materials have high rate of mass retention on impact and, therefore, should not bias the estimated mass ratio of late accreted materials for the Earth/Mars/Moon system. Based on the best results of Monte-Carlo code simulation (Bottke *et al.*, 2010), the HSE were delivered to the Earth and Moon systems via a few large projectiles with mean diameters of 2500 to 3000 km and 250 to 300 km, respectively. This is also consistent with the observation that, in the absence of plate tectonics, the impactors needed to be large enough to breach early planetary lithosphere, create local magma ponds or lakes from their impact energy, and then efficiently mix into the mantle, but not so large that their impact-fragmented cores coalesced with the Earth's core (Dahl and Stevenson, 2010). Assuming Earth to be in a magma ocean phase at the time of the impact, the iron core of a differentiated projectile that is assumed to be half of the projectile's diameter, will likely become emulsified into the mantle if it is smaller than the depth of the magma ocean (Bottke *et al.*, 2010; Dahl and Stevenson, 2010). For Earth, this criterion limits HSE delivery among differentiated projectiles to diameters <4000 km (Rubie *et al.*, 2003).

The differentiated projectiles would likely consist of HSE-rich cores and HSE-stripped silicate mantles. Upon impact, the cores will likely emulsify in a magma ocean, whereas the silicate mantles will not. As a result, domains with low HSE abundances and positive ^{182}W anomalies would be expected to have been created. In the absence of modern-style plate tectonics, the silicate domains would likely have survived for extended periods of time before being homogenized within the mantle via whole-mantle convection. This model, which requires delivery of the bulk of late accreted materials prior to 4.40 Ga, is consistent with the observation of an absence of trend of increasing HSE abundances in komatiitic sources from

943 3.5 to 2.7 Ga. It is also consistent with the large, non-systematic variations in HSE
944 abundances between individual both early and late Archean komatiite systems (Fig. 11).
945 A stagnant, or episodic, subduction regime in the Hadean is consistent with the available
946 observations (O'Neill and Debaille, 2014) and was most likely the mechanism that was
947 responsible for the slow mixing of late accreted materials into the mantle. These observations
948 include mantle mixing constraints (long residence time of isotope anomalies and
949 compositional heterogeneities) and thermal history models (higher rates of internal heat
950 production versus lower heat flux to avoid the "Archean thermal catastrophe"). These also
951 include basic geologic data, such as formation of early Archean TTGs and presence of
952 greenstone sequences with interleaving island arc and plume-derived lavas. It can explain the
953 worldwide preservation of ^{142}Nd anomalies in the 4.2-2.7 Ga geological record and their
954 complete disappearance in the post-Archean (Debaille *et al.*, 2013). Apparently, W isotope
955 heterogeneities were more resilient to the mantle homogenization processes compared to
956 those of Nd, as evidenced by the presence of large ^{182}W anomalies in recent and modern
957 plume-derived lavas (Rizo *et al.*, 2016a; Mundl *et al.*, 2017); this could be due to the different
958 nature of these heterogeneities, as well as different location of their respective mantle sources.

959 **6. Conclusions**

960 The 2.72 Ga Boston Creek komatiitic basalt lava flow (BCF) in the Abitibi greenstone
961 belt is characterized by a positive ^{182}W anomaly, chondritic ^{187}Os/^{188}Os isotopic composition
962 and low calculated absolute HSE abundances in its mantle source, a set of geochemical
963 features that are collectively unique among the komatiite systems studied so far. When
964 considered together, these constraints require derivation of the parental BCF magma from a
965 mantle source that formed very early in Earth's history and received only a fraction of the
966 present-day mantle HSE complement before becoming isolated until the time of komatiite
967 emplacement. These data provide new evidence for the highly heterogeneous nature of the

Archean mantle in terms of absolute HSE abundances, consistent with stochastic late accretion of a limited number of sizable impactors into the mantle. The survival of the early-formed BCF mantle source for ≥1.8 billion years implies that portions of the mantle remained poorly mixed with regard to HSE and W until at least the late Archean.

Acknowledgements

This work was supported by NSF Petrology and Geochemistry grant EAR 1447174 to ISP, NSF-CSEDI grant EAR 1265169 to RJW, ANR grant ANR-10-BLANC-0603 M&Ms – Mantle Melting – Measurements, Models, Mechanisms to JBT, and NSF-IF grant EAR 0549300, which provided partial support for the *Triton* mass-spectrometer used for most of the measurements in this study. We are grateful to Valentina Puchtel and Richard Ash for help with preparation of samples and ICP-MS measurements at the *IGL* and *PL*, and to Philippe Telouk for maintenance of the MC-ICP-MS in Lyon. Mike Lesher is thanked for guidance during field work in the Kirkland Lake area.

983 **References**

984 Alard, O., Griffin, W.L., Lorand, J.-P., Jackson, S.E., and O'Reilly, S.Y., 2000. Non-
985 chondritic distribution of the highly siderophile elements in mantle sulfides. Nature
986 **407**(6806): 891-894.
987 Archer, G.J., Mundl, A., Walker, R.J., Worsham, E.A., and Bermingham, K.R., 2017. High-
988 precision analysis of $^{182}W/^{184}W$ and $^{183}W/^{184}W$ by negative thermal ionization mass
989 spectrometry: Per-integration oxide corrections using measured $^{18}O/^{16}O$.
990 INTERNATIONAL JOURNAL OF MASS SPECTROMETRY **414**: 80-86.
991 Arevalo, R., and McDonough, W.F., 2008. Tungsten geochemistry and implications for
992 understanding the Earth's interior. Earth and Planetary Science Letters **272**(3-4): 656-
993 665.
994 Arndt, N.T., 1977. Thick, layered peridotite-gabbro lava flows in Munro Township, Ontario.
995 Canadian Journal of Earth Sciences **14**(11): 2620-2637.
996 Arndt, N.T., 1986. Differentiation of komatiite flows. Journal of Petrology **27**(2): 279-301.
997 Arndt, N.T. (1994). Archean komatiites. Archean Crustal Evolution. Condie, K.C.
998 Amsterdam, Elsevier**:** 11-44.
999 Arndt, N.T., Lesher, C.M., and Barnes, S.J. (2008). Komatiite. Cambridge, UK, Cambridge
1000 University Press.
1001 Arndt, N.T., Naldrett, A.J., and Pyke, D.R., 1977. Komatiitic and iron-rich tholeiitic lavas of
1002 Munro Township, northeast Ontario. Journal of Petrology **18**: 319-369.
1003 Arndt, N.T., and Nesbitt, R.W. (1984). Magma mixing in komatiitic lavas from Munro
1004 Township, Ontario. Archaean Geochemistry. Kröner, A. Berlin-Heidelberg**:** 99-114.
1005 Babechuk, M.G., Kamber, B.S., Greig, A., Canil, D., and Kodolanyi, J., 2010. The behaviour
1006 of tungsten during mantle melting revisited with implications for planetary
1007 differentiation time scales. Geochimica et Cosmochimica Acta **74**(4): 1448-1470.
1008 Barley, M.E., Kerrich, R., Reudavy, I., and Xie, Q., 2000. Late Archaean Ti-rich, Al-depleted
1009 komatiites and komatiitic volcaniclastic rocks from the Murchison Terrane in Western
1010 Australia. Australian Journal of Earth Sciences **47**(5): 873-883.
1011 Barnes, S.-J., Naldrett, A.J., and Gorton, M.P., 1985. The origin of the fractionation of
1012 platinum-group elements in terrestrial magmas. Chemical Geology **53**(3-4): 303-323.
1013 Barnes, S.-J., and Often, M., 1990. Ti-rich komatiites from Northern Norway. Contributions
1014 to Mineralogy and Petrology **105**(1): 42-54.
1015 Barnes, S.J., and Fiorentini, M.L., 2008. Iridium, ruthenium and rhodium in komatiites:
1016 Evidence for iridium alloy saturation. Chemical Geology **257**(1-2): 44-58.
1017 Becker, H., Horan, M.F., Walker, R.J., Gao, S., Lorand, J.-P., and Rudnick, R.L., 2006.
1018 Highly siderophile element composition of the Earth's primitive upper mantle:
1019 Constraints from new data on peridotite massifs and xenoliths. Geochimica et
1020 Cosmochimica Acta **70**(17): 4528-4550.
1021 Bennett, V.C., Brandon, A.D., and Nutman, A.P., 2007. Coupled ^{142}Nd-^{143}Nd isotopic
1022 evidence for Hadean mantle dynamics. Science **318**(5858): 1907-1910.
1023 Birck, J.L., Roy-Barman, M., and Capman, F., 1997. Re-Os isotopic measurements at the
1024 femtomole level in natural samples. Geostandards Newsletter **20**(1): 19-27.
1025 Blichert-Toft, J., 2001. On the Lu-Hf isotope geochemistry of silicate rocks. Geostandards
1026 Newsletter-the Journal of Geostandards and Geoanalysis **25**(1): 41-56.
1027 Blichert-Toft, J., and Albarède, F., 1997. The Lu-Hf isotope geochemistry of chondrites and
1028 the evolution of the mantle-crust system. Earth and Planetary Science Letters **148**(1-
1029 2): 243-258.

Blichert-Toft, J., Boyet, M., Telouk, P., and Albarede, F., 2002. ^{147}Sm-^{143}Nd and ^{176}Lu-^{176}Hf in eucrites and the differentiation of the HED parent body. Earth and Planetary Science Letters **204**(1-2): 167-181.

Blichert-Toft, J., Chauvel, C., and Albaréde, F., 1997. Separation of Hf and Lu for high-precision isotope analysis of rock samples by magnetic sector multiple collector ICP-MS. Contributions to Mineralogy and Petrology **127**(3): 248-260.

Blichert-Toft, J., and Puchtel, I.S., 2010. Depleted mantle sources through time: Evidence from Lu-Hf and Sm-Nd isotope systematics of Archean komatiites. Earth and Planetary Science Letters **297**(3-4): 598-606.

Borg, L.E., Gaffney, A.M., and Shearer, C.K., 2014. A review of lunar chronology revealing a preponderance of 4.34–4.37 Ga ages. Meteoritics and Planetary Science **50**(4): 715-732.

Bottke, W.F., Levison, H.F., Nesvorny, D., and Dones, L., 2007. Can planetesimals left over from terrestrial planet formation produce the lunar Late Heavy Bombardment? Icarus **190**(1): 203-223.

Bottke, W.F., Morbidelli, A., Jedicke, R., Petit, J.-M., Levison, H.F., Michel, P., and Metcalfe, T.S., 2002. Debiased Orbital and Absolute Magnitude Distribution of the Near-Earth Objects. Icarus **156**(2): 399-433.

Bottke, W.F., Walker, R.J., Day, J.M.D., Nesvorny, D., and Elkins-Tanton, L., 2010. Stochastic Late Accretion to Earth, the Moon, and Mars. Science **330**(6010): 1527-1530.

Bouvier, A., Vervoort, J.D., and Patchett, P.J., 2008. The Lu-Hf and Sm-Nd isotopic composition of CHUR: Constraints from unequilibrated chondrites and implications for the bulk composition of terrestrial planets. Earth and Planetary Science Letters **273**(1-2): 48-57.

Boyet, M., Blichert-Toft, J., Rosing, M., Storey, M., Télouk, P., and Albarède, F., 2003. ^{142}Nd evidence for early Earth differentiation. Earth and Planetary Science Letters **214**: 427-442.

Boyet, M., and Carlson, R.W., 2005. ^{142}Nd evidence for early (> 4.53 Ga) global differentiation of the silicate Earth. Science **309**(5734): 576-581.

Boyet, M., and Carlson, R.W., 2006. A new geochemical model for the Earth's mantle inferred from ^{146}Sm-^{142}Nd systematics. Earth and Planetary Science Letters **250**(1-2): 254-268.

Brandon, A.D., Humayun, M., Puchtel, I.S., and Zolensky, M., 2005. Re-Os isotopic systematics and platinum group element composition of the Tagish Lake carbonaceous chondrite. Geochimica et Cosmochimica Acta **69**(6): 1619-1631.

Brandon, A.D., Puchtel, I.S., Walker, R.J., Day, J.M.D., Irving, A.J., and Taylor, L.A., 2012. Evolution of the martian mantle Inferred from the ^{187}Re-^{187}Os isotope and highly siderophile element abundance systematics of shergottite meteorites. Geochimica et Cosmochimica Acta **76**(1): 206-235.

Brenan, J.M., McDonough, W.F., and Dalpé, C., 2003. Experimental constraints on the partitioning of rhenium and some platinum-group elements between olivine and silicate melt. Earth and Planetary Science Letters **212**(1-2): 135-150.

Canup, R.M., 2004. Simulations of a late lunar-forming impact. Icarus **168**(2): 433-456.

Canup, R.M., 2012. Forming a Moon with an Earth-like Composition via a Giant Impact. Science **338**(6110): 1052-1055.

Canup, R.M., and Asphaug, E., 2001. Origin of the Moon in a giant impact near the end of the Earth's formation. Nature **412**(6848): 708-712.

Capdevila, R., Arndt, N.T., Letendre, J., and Sauvage, J.-F., 1999. Diamonds in volcaniclastic komatiite from French Guiana. Nature **399**(6735): 456-458.

1080 Carlson, R.W., and Boyet, M., 2008. Composition of the Earth's interior: the importance of
1081 early events. Philosophical Transactions of the Royal Society a-Mathematical Physical
1082 and Engineering Sciences **366**(1883): 4077-4103.
1083 Caro, G., Bourdon, B., Birck, J.-L., and Moorbath, S., 2006. High-precision $^{142}Nd/^{144}Nd$
1084 measurements in terrestrial rocks: Constraints on the early differentiation of the
1085 Earth's mantle. Geochimica et Cosmochimica Acta **70**(1): 164-191.
1086 Caro, G., Bourdon, B., Birck, J.L., and Moorbath, S., 2003. ^{146}Sm-^{142}Nd evidence from Isua
1087 metamorphosed sediments for early differentiation of the Earth's mantle. Nature
1088 **423**(6938): 428-432.
1089 Caro, G., Morino, P., Mojzsis, S.J., Cates, N.L., and Bleeker, W., 2017. Sluggish Hadean
1090 geodynamics: Evidence from coupled $^{146,147}Sm$-$^{142,143}Nd$ systematics in Eoarchean
1091 supracrustal rocks of the Inukjuak domain (Québec). Earth and Planetary Science
1092 Letters **457**: 23-37.
1093 Cattell, A., and Arndt, N.T., 1987. Low- and high-alumina komatiites from a Late Archaean
1094 sequence, Newton Township, Ontario. Contributions to Mineralogy and Petrology
1095 **97**(2): 218-227.
1096 Chou, C.-L., Shaw, D.M., and Crocket, J.H., 1983. Siderophile trace elements in the Earth's
1097 oceanic crust and upper mantle. Journal of Geophysical Research **88**(S2): A507-A518.
1098 Cohen, A.S., and Waters, F.G., 1996. Separation of osmium from geological materials by
1099 solvent extraction for analysis by thermal ionisation mass spectrometry. Analytica
1100 Chimica Acta **332**(2-3): 269-275.
1101 Corfu, F., and Noble, S.R., 1992. Genesis of the southern Abitibi greenstone belt, Superior
1102 Province, Canada: Evidence from zircon Hf-isotope analyses using a single filament
1103 technique. Geochimica et Cosmochimica Acta **56**(5): 2081-2097.
1104 Creaser, R.A., Papanastassiou, D.A., and Wasserburg, G.J., 1991. Negative Thermal Ion
1105 Mass-Spectrometry of Osmium, Rhenium, and Iridium. Geochimica et Cosmochimica
1106 Acta **55**(1): 397-401.
1107 Dahl, T.W., and Stevenson, D.J., 2010. Turbulent mixing of metal and silicate during planet
1108 accretion - And interpretation of the Hf-W chronometer. Earth and Planetary Science
1109 Letters **295**(1-2): 177-186.
1110 Dale, C.W., Kruijer, T.S., and Burton, K.W., 2017. Highly siderophile element and ^{182}W
1111 evidence for a partial late veneer in the source of 3.8 Ga rocks from Isua, Greenland.
1112 Earth and Planetary Science Letters **458**: 394-404.
1113 Dale, C.W., Macpherson, C.G., Pearson, D.G., Hammond, S.J., and Arculus, R.J., 2012. Inter-
1114 element fractionation of highly siderophile elements in the Tonga Arc due to flux
1115 melting of a depleted source. Geochimica et Cosmochimica Acta **89**(Supplement C):
1116 202-225.
1117 Dauphas, N., Burkhardt, C., Warren, P.H., and Fang-Zhen, T., 2014. Geochemical arguments
1118 for an Earth-like Moon-forming impactor. Philosophical Transactions of the Royal
1119 Society A: Mathematical, Physical and Engineering Sciences
1120 **372**(2024): 20130244.
1121 Day, J.M.D., Brandon, A.D., and Walker, R.J., 2016. Highly Siderophile Elements in Earth,
1122 Mars, the Moon, and Asteroids. Reviews in Mineralogy and Geochemistry **81**(1): 161-
1123 238.
1124 Day, J.M.D., Pearson, D.G., and Taylor, L.A., 2007. Highly siderophile element constraints
1125 on accretion and differentiation of the Earth-Moon system. Science **315**(5809): 217-
1126 219.
1127 Day, J.M.D., and Walker, R.J., 2015. Highly siderophile element depletion in the Moon. Earth
1128 and Planetary Science Letters **423**: 114-124.

Debaille, V., O'Neill, C., Brandon, A.D., Haenecour, P., Yin, Q.-Z., Mattielli, N., and Treiman, A.H., 2013. Stagnant-lid tectonics in early Earth revealed by ^{142}Nd variations in late Archean rocks. Earth and Planetary Science Letters **373**: 83-92.

Donaldson, C.H., 1979. An experimental investigation of the delay in nucleation of olivine in Mafic Magmas. Contributions to Mineralogy and Petrology **69**(1): 21-32.

Fischer-Gödde, M., and Becker, H., 2012. Osmium isotope and highly siderophile element constraints on ages and nature of meteoritic components in ancient lunar impact rocks. Geochimica et Cosmochimica Acta **77**: 135-156.

Fischer-Gödde, M., Becker, H., and Wombacher, F., 2010. Rhodium, gold and other highly siderophile element abundances in chondritic meteorites. Geochimica et Cosmochimica Acta **74**(1): 356-379.

Fischer-Gödde, M., Becker, H., and Wombacher, F., 2011. Rhodium, gold and other highly siderophile elements in orogenic peridotites and peridotite xenoliths. Chemical Geology **280**(3-4): 365-383.

Fonseca, R.O.C., Laurenz, V., Mallmann, G., Luguet, A., Hoehne, N., and Jochum, K.P., 2012. New constraints on the genesis and long-term stability of Os-rich alloys in the Earth's mantle. Geochimica et Cosmochimica Acta **87**: 227-242.

Fonseca, R.O.C., Mallmann, G., O'Neill, H.S.C., Campbell, I.H., and Laurenz, V., 2011. Solubility of Os and Ir in sulfide melt: Implications for Re/Os fractionation during mantle melting. Earth and Planetary Science Letters **311**(3-4): 339-350.

Foster, J.G., Lambert, D.D., Frick, L.R., and Maas, R., 1996. Re-Os isotopic evidence for genesis of Archaean nickel ores from uncontaminated komatiites. Nature **382**(6593): 703-706.

Green, J.C., and Shulz, K.J., 1977. Iron-rich basaltic komatiites in the Early Precambrian Vermilion district, Minnesota. Canadian Journal of Earth Sciences **14**(10): 2181-2192.

Hamilton, P.J., O'Nions, R.K., Bridgwater, D., and Nutman, A.P., 1983. Sm-Nd studies of Archaean metasediments and metavolcanics from West Greenland and their implications for the Earth's early history. Earth and Planetary Science Letters **62**(2): 263-272.

Hanski, E., Huhma, H., Rastas, P., and Kamenetsky, V.S., 2001. The Paleoproterozoic komatiite-picrite association of Finnish Lapland. Journal of Petrology **42**(5): 855-876.

Herzberg, C., and O'Hara, M.J., 2002. Plume-associated ultramafic magmas of Phanerozoic age. Journal of Petrology **43**(10): 1857-1883.

Herzberg, C.T., 1992. Depth and degree of melting of komatiites. Journal of Geophysical Research **97**(B4): 4521-4540.

Herzberg, C.T., and Ohtani, E., 1988. Origin of komatiite at high pressures. Earth and Planetary Science Letters **88**(3-4): 321-329.

Hofmann, A.W., 1988. Chemical differentiation of the Earth: The relationship between mantle, continental crust and oceanic crust. Earth and Planetary Science Letters **90**(3): 297-314.

Hollings, P., and Wyman, D., 1999. Trace element and Sm-Nd systematics of volcanic and intrusive rocks from the 3 Ga Lumby Lake Greenstone belt, Superior Province: evidence for Archean plume-arc interaction. Lithos **46**(2): 189-213.

Horan, M.F., Walker, R.J., Morgan, J.W., Grossman, J.N., and Rubin, A.E., 2003. Highly siderophile elements in chondrites. Chemical Geology **196**(1-4): 5-20.

Jacobsen, S.B., and Wasserburg, G.J., 1980. Sm-Nd isotopic evolution of chondrites. Earth and Planetary Science Letters **50**(1): 139-155.

Jensen, L.S., and Pyke, D.R. (1982). Komatiites in the Ontario portion of the Abitibi belt. Komatiites. Arndt, N.T. and Nisbet, E.G. London, George Allen and Unwin**:** 147-158.

1178 Jolly, W.T., 1980. Development and degradation of Archean lavas, Abitibi area, Canada, in
1179 light of major-element geochemistry. Journal of Petrology **21**(2): 323-363.
1180 Keays, R.R., 1995. The role of komatiitic and picritic magmatism and S-saturation in the
1181 formation of ore deposits. Lithos **34**(1-3): 1-18.
1182 Kimura, K., Lewis, R.S., and Anders, S., 1974. Distribution of gold and rhenium between
1183 nickel-iron and silicate melts; implications for abundance of siderophile elements on
1184 the Earth and Moon. Geochimica et Cosmochimica Acta **38**(5): 683-701.
1185 Kleine, T., Mezger, K., Münker, C., Palme, H., and Bischoff, A., 2004a. ^{182}Hf-^{182}W isotope
1186 systematics of chondrites, eucrites, and martian meteorites: Chronology of core
1187 formation and early mantle differentiation in Vesta and Mars. Geochimica et
1188 Cosmochimica Acta **68**(13): 2935-2946.
1189 Kleine, T., Mezger, K., Palme, H., and Münker, C., 2004b. The W isotope evolution of the
1190 bulk silicate Earth: constraints on the timing and mechanisms of core formation and
1191 accretion. Earth and Planetary Science Letters **228**(1-2): 109-123.
1192 Kleine, T., Münker, C., Mezger, K., and Palme, H., 2002. Rapid accretion and early core
1193 formation on asteroids and the terrestrial planets from Hf-W chronometry. Nature
1194 **418**(6901): 952-955.
1195 Kleine, T., Touboul, M., Bourdon, B., Nimmo, F., Mezger, K., Palme, H., Jacobsen, S.B.,
1196 Yin, Q.-Z., and Halliday, A.N., 2009. Hf-W chronology of the accretion and early
1197 evolution of asteroids and terrestrial planets. Geochimica et Cosmochimica Acta
1198 **73**(17): 5150-5188.
1199 Kleine, T., and Walker, R.J., 2017. Tungsten Isotopes in Planets. Annual Review of Earth and
1200 Planetary Sciences **45**(1): 389-417.
1201 König, S., Münker, C., Hohl, S., Paulick, H., Barth, A.R., Lagos, M., Pfander, J., and Büchl,
1202 A., 2011. The Earth's tungsten budget during mantle melting and crust formation.
1203 Geochimica et Cosmochimica Acta **75**(8): 2119-2136.
1204 Kruijer, T.S., and Kleine, T., 2017. Tungsten isotopes and the origin of the Moon. Earth and
1205 Planetary Science Letters **475**(Supplement C): 15-24.
1206 Kruijer, T.S., Kleine, T., Borg, L.E., Brennecka, G.A., Irving, A.J., Bischoff, A., and Agee,
1207 C.B., 2017. The early differentiation of Mars inferred from Hf-W chronometry. Earth
1208 and Planetary Science Letters **474**(Supplement C): 345-354.
1209 Kruijer, T.S., Kleine, T., Fischer-Gödde, M., and Sprung, P., 2015. Lunar tungsten isotopic
1210 evidence for the late veneer. Nature **520**(7548): 534-537.
1211 Lofgren, G.E., 1983. Effect of Heterogeneous Nucleation on Basaltic Textures: A Dynamic
1212 Crystallization Study. Journal of Petrology **24**(3): 229-255.
1213 Lorand, J.-P., and Alard, O., 2001. Platinum-group element abundances in the upper mantle:
1214 new constraints from in situ and whole-rock analyses of Massif Central xenoliths
1215 (France). Geochimica et Cosmochimica Acta **65**(16): 2789-2806.
1216 Ludwig, K.R. (2003). ISOPLOT 3.00. A geochronological toolkit for Microsoft Excel.
1217 Berkeley Geochronology Center Spec. Publ. **No. 4:** 70 pp.
1218 Luguet, A., Shirey, S.B., Lorand, J.-P., Horan, M.F., and Carlson, R.W., 2007. Residual
1219 platinum-group minerals from highly depleted harzburgites of the Lherz massif
1220 (France) and their role in HSE fractionation of the mantle. Geochimica et
1221 Cosmochimica Acta **71**(12): 3082-3097.
1222 Maier, W.D., Barnes, S.J., Campbell, I.H., Fiorentini, M.L., Peltonen, P., Barnes, S.J., and
1223 Smithies, R.H., 2009. Progressive mixing of meteoritic veneer into the early Earth's
1224 deep mantle. Nature **460**(7255): 620-623.
1225 Mavrogenes, J.A., and O'Neill, H.S.C., 1999. The relative effects of pressure, temperature and
1226 oxygen fugacity on the solubility of sulfide in mafic magmas. Geochimica et
1227 Cosmochimica Acta **63**(7-8): 1173-1180.

McDonough, W.F. (2004). Compositional model for the Earth's core. Treatise on Geochemistry. Amsterdam, Elsevier. **2:** 547-568.
Meisel, T., and Moser, J., 2004. Platinum-group element and rhenium concentrations in low-abundance reference materials. GEOSTANDARDS AND GEOANALYTICAL RESEARCH **28**(2): 233-250.
Meisel, T., Walker, R.J., Irving, A.J., and Lorand, J.-P., 2001. Osmium isotopic compositions of mantle xenoliths: A global perspective. Geochimica et Cosmochimica Acta **65**(8): 1311-1323.
Mertzman, S.A., 2000. K-Ar results from the southern Oregon - northern California Cascade range. Oregon Geology **62**(4): 99-122.
Morgan, J.W., 1985. Osmium isotope constraints on Earth's late accretionary history. Nature **317**(6039): 703-705.
Morgan, J.W., Ganapathy, R., Higuchi, H., and Anders, E. (1977). Meteoritic Material on the Moon. The Soviet-American Conference on Cosmochemistry of the Moon, Washington, DC, NASA SP-370, US Govt. Printing Office.
Morgan, J.W., Wanderless, G.A., Petrie, R.K., and Irving, A.J., 1981. Composition of the earth's upper mantle, I. Siderophile trace elements in ultramafic nodules. Tectonophysics **75**(1-2): 47-67.
Mundl, A., Touboul, M., Jackson, M.G., Day, J.M.D., Kurz, M.D., Lekic, V., Helz, R.T., and Walker, R.J., 2017. Tungsten-182 heterogeneity in modern ocean island basalts. Science **356**(6333): 66-69.
Nesbitt, R.W., Sun, S.S., and Purvis, A.C., 1979. Komatiites: geochemistry and genesis. Canadian Mineralogist **17**(2): 165-186.
Norman, M.D., 2005. Lunar impact breccias: Petrology, crater setting, and bombardment history of the Moon. Australian Journal of Earth Sciences **52**(4-5): 711-723.
Norman, M.D., Bennett, V.C., and Ryder, G., 2002. Targeting the impactors: siderophile element signatures of lunar impact melts from Serenitatis. Earth and Planetary Science Letters **202**(2): 217-228.
O'Neil, J., Carlson, R.W., Francis, D., and Stevenson, R.K., 2008. Neodymium-142 evidence for Hadean mafic crust. Science **321**(5897): 1828-1831.
O'Neil, J., Carlson, R.W., Paquette, J.-L., and Francis, D., 2012. Formation age and metamorphic history of the Nuvvuagittuq Greenstone Belt. Precambrian Research **220-221**: 23-44.
O'Neil, J., Rizo, H., Boyet, M., Carlson, R.W., and Rosing, M.T., 2016. Geochemistry and Nd isotopic characteristics of Earth's Hadean mantle and primitive crust. Earth and Planetary Science Letters **442**: 194-205.
O'Neill, C., and Debaille, V., 2014. The evolution of Hadean-Eoarchaean geodynamics. Earth and Planetary Science Letters **406**: 49-58.
Ohtani, E., 1984. Generation of komatiite magma and gravitational differentiation in the deep upper mantle. Earth and Planetary Science Letters **67**(2): 261-272.
Ohtani, E., 1990. Majorite fractionation and genesis of komatiites in the deep mantle. Precambrian Research **48**(3): 195-202.
Puchtel, I.S., Blichert-Toft, J., Touboul, M., Horan, M.F., and Walker, R.J., 2016a. The coupled ^{182}W-^{142}Nd record of early terrestrial mantle differentiation. Geochemistry, Geophysics, Geosystems **17**(6): 2168-2193.
Puchtel, I.S., Blichert-Toft, J., Touboul, M., Walker, R.J., Byerly, G., Nisbet, E.G., and Anhaeusser, C.R., 2013. Insights into early Earth from Barberton komatiites: Evidence from lithophile isotope and trace element systematics. Geochimica et Cosmochimica Acta **108**: 63-90.

Puchtel, I.S., Brandon, A.D., and Humayun, M., 2004a. Precise Pt-Re-Os isotope systematics of the mantle from 2.7-Ga komatiites. Earth and Planetary Science Letters **224**(1-2): 157-174.

Puchtel, I.S., Brandon, A.D., Humayun, M., and Walker, R.J., 2005. Evidence for the early differentiation of the core from Pt-Re-Os isotope systematics of 2.8-Ga komatiites. Earth and Planetary Science Letters **237**(1-2): 118-134.

Puchtel, I.S., and Humayun, M., 2005. Highly siderophile element geochemistry of ^{187}Os-enriched 2.8-Ga Kostomuksha komatiites, Baltic Shield. Geochimica et Cosmochimica Acta **69**(6): 1607-1618.

Puchtel, I.S., Humayun, M., Campbell, A., Sproule, R., and Lesher, C.M., 2004b. Platinum group element geochemistry of komatiites from the Alexo and Pyke Hill areas, Ontario, Canada. Geochimica et Cosmochimica Acta **68**(6): 1361-1383.

Puchtel, I.S., Humayun, M., and Walker, R.J., 2007. Os-Pb-Nd isotope and highly siderophile and lithophile trace element systematics of komatiitic rocks from the Volotsk suite, SE Baltic Shield. Precambrian Research **158**(1-2): 119-137.

Puchtel, I.S., Touboul, M., Blichert-Toft, J., Walker, R.J., Brandon, A.D., Nicklas, R.W., Kulikov, V.S., and Samsonov, A.V., 2016b. Lithophile and siderophile element systematics of the mantle at the Archean-Proterozoic boundary: Evidence from 2.4 Ga komatiites. Geochimica et Cosmochimica Acta **180**: 227-255.

Puchtel, I.S., Walker, R.J., Anhaeusser, C.R., and Gruau, G., 2009a. Re-Os isotope systematics and HSE abundances of the 3.5 Ga Schapenburg komatiites, South Africa: Hydrous melting or prolonged survival of primordial heterogeneities in the mantle? Chemical Geology **262**(3-4): 355-369.

Puchtel, I.S., Walker, R.J., Brandon, A.D., and Nisbet, E.G., 2009b. Pt-Re-Os and Sm-Nd isotope and HSE and REE systematics of the 2.7 Ga Belingwe and Abitibi komatiites. Geochimica et Cosmochimica Acta **73**(20): 6367-6389.

Puchtel, I.S., Walker, R.J., James, O.B., and Kring, D.A., 2008. Osmium isotope and highly siderophile element systematics of lunar impact melt breccias: Implications for the late accretion history of the Moon and Earth. Geochimica et Cosmochimica Acta **72**(12): 3022-3042.

Puchtel, I.S., Walker, R.J., Touboul, M., Nisbet, E.G., and Byerly, G.R., 2014. Insights into Early Earth from the Pt-Re-Os isotope and Highly Siderophile Element abundance systematics of Barberton komatiites. Geochimica et Cosmochimica Acta **125**: 394-413.

Rehkämper, M., and Halliday, A.N., 1997. Development and application of new ion-exchange techniques for the separation of the platinum-group and other siderophile elements from geological samples. Talanta **44**(4): 663-672.

Righter, K., Walker, R.J., and Warren, P.H. (2000). Significance of highly siderophile elements and osmium isotopes in the lunar and terrestrial mantles. Origin of the Earth and Moon. Righter, K. and Canup, R.M. Tucson, University of Arizona Press**:** 291-322.

Ringwood, A.E., 1992. Volatile and siderophile element geochemistry of the Moon: a reappraisal. Earth and Planetary Science Letters **111**(2): 537-555.

Rizo, H., Boyet, M., Blichert-Toft, J., O'Neil, J., Rosing, M.T., and Paquette, J.-L., 2012. The elusive Hadean enriched reservoir revealed by ^{142}Nd deficits in Isua Archaean rocks. Nature **491**(7422): 96-100.

Rizo, H., Boyet, M., Blichert-Toft, J., and Rosing, M., 2011. Combined Nd and Hf isotope evidence for deep-seated source of Isua lavas. Earth and Planetary Science Letters **312**(3-4): 267-279.

Rizo, H., Boyet, M., Blichert-Toft, J., and Rosing, M.T., 2013. Early mantle dynamics inferred from ^{142}Nd variations in Archean rocks from southwest Greenland. Earth and Planetary Science Letters **377-378**: 324-335.

Rizo, H., Walker, R.J., Carlson, R.W., Horan, M.F., Mukhopadhyay, S., Manthos, V., Francis, D., and Jackson, M.G., 2016a. Preservation of Earth-forming events in the tungsten isotopic composition of modern flood basalts. Science **352**(6287): 809-812.

Rizo, H., Walker, R.J., Carlson, R.W., Touboul, M., Horan, M.F., Puchtel, I.S., Boyet, M., and Rosing, M.T., 2016b. Early Earth differentiation investigated through ^{142}Nd, ^{182}W, and highly siderophile element abundances in samples from Isua, Greenland. Geochimica et Cosmochimica Acta **175**: 319-336.

Roth, A.S.G., Bourdon, B., Mojzsis, S.J., Touboul, M., Sprung, P., Guitreau, M., and Blichert-Toft, J., 2013. Inherited ^{142}Nd anomalies in Eoarchean protoliths. Earth and Planetary Science Letters **361**: 50-57.

Rubie, D.C., Melosh, H.J., Reid, J.E., Liebske, C., and Righter, K., 2003. Mechanisms of metal-silicate equilibration in the terrestrial magma ocean. Earth and Planetary Science Letters **205**(3-4): 239-255.

Scherer, E., Münker, C., and Mezger, K., 2001. Calibration of the lutetium-hafnium clock. Science **293**(5530): 683-687.

Schoenberg, R., Kamber, B.S., Collerson, K.D., and Eugster, O., 2002. New W-isotope evidence for rapid terrestrial accretion and very early core formation. Geochimica et Cosmochimica Acta **66**(17): 3151-3160.

Schulz, K.J. (1982). Magnesian basalts from the Archean terrains of Minnesota. Komatiites. Arndt, N.T. and Nisbet, E.G. London, George Allen and Unwin**:** 171-186.

Shirey, S.B., and Walker, R.J., 1998. The Re-Os isotope system in cosmochemistry and high-temperature geochemistry. Annual Reviews of Earth and Planetary Sciences **26**: 423-500.

Smoliar, M.I., Walker, R.J., and Morgan, J.W., 1996. Re-Os ages of Group IIA, IIIA, IVA, and IVB iron meteorites. Science **271**(5762): 1099-1102.

Söderlund, U., Patchett, J.P., Vervoort, J.D., and Isachsen, C.E., 2004. The ^{176}Lu decay constant determined by Lu-Hf and U-Pb isotope systematics of Precambrian mafic intrusions. Earth and Planetary Science Letters **219**(3-4): 311-324.

Stone, W.E., Crocket, J.H., Dickin, A.P., and Fleet, M.E., 1995a. Origin of Archean ferropicrites: geochemical constraints from the Boston Creek Flow, Abitibi greenstone belt, Ontario, Canada. Chemical Geology **121**(1-4): 51-71.

Stone, W.E., Crocket, J.H., and Fleet, M.E., 1995b. Differentiation processes in an unusual iron-rich alumina-poor Archean ultramafic/mafic igneous body, Ontario. Contributions to Mineralogy and Petrology **119**(2-3): 287-300.

Stone, W.E., Jensen, L.S., and Church, W.R., 1987. Petrography and geochemistry of an unusual Fe-rich basaltic komatiite from Boston Township, Northeastern Ontario. Canadian Journal of Earth Sciences **24**(12): 2537-2550.

Tomlinson, K.Y., Hughes, D.J., Thurston, P.C., and Hall, R.P., 1999. Plume magmatism and crustal growth at 2.9 to 3.0 Ga in the Steep Rock and Lumby Lake area, Western Superior Province. Lithos **46**(1): 103-136.

Touboul, M., Kleine, T., Bourdon, B., Palme, H., and Wieler, R., 2007. Late formation and prolonged differentiation of the Moon inferred from W isotopes in lunar metals. Nature **450**(7173): 1206-1209.

Touboul, M., Liu, J., O'Neil, J., Puchtel, I.S., and Walker, R.J., 2014. New Insights into the Hadean Mantle Revealed by ^{182}W and Highly Siderophile Element Abundances of Supracrustal Rocks from the Nuvvuagittuq Greenstone Belt, Quebec, Canada. Chemical Geology(383): 63-75.

Touboul, M., Puchtel, I.S., and Walker, R.J., 2012. ^{182}W Evidence for Long-Term Preservation of Early Mantle Differentiation Products. Science **335**: 1065-1069.

Touboul, M., Puchtel, I.S., and Walker, R.J., 2015. Tungsten isotopic evidence for disproportional late accretion to the Earth and Moon. Nature **520**(7548): 530-533.

Touboul, M., and Walker, R.J., 2012. High precision tungsten isotope measurement by thermal ionization mass spectrometry. INTERNATIONAL JOURNAL OF MASS SPECTROMETRY **309**: 109-117.

Walker, R.J., 2009. Highly siderophile elements in the Earth, Moon and Mars: Update and implications for planetary accretion and differentiation. Chemie der Erde - Geochemistry **69**(2): 101-125.

Walker, R.J., 2014. Siderophile element constraints on the origin of the Moon. PHILOSOPHICAL TRANSACTIONS OF THE ROYAL SOCIETY OF LONDON **372**: 20130258.

Walker, R.J., Horan, M.F., Morgan, J.W., Becker, H., Grossman, J.N., and Rubin, A.E., 2002. Comparative ^{187}Re-^{187}Os systematics of chondrites: Implications regarding early solar system processes. Geochimica et Cosmochimica Acta **66**(23): 4187-4201.

Walker, R.J., Horan, M.F., Shearer, C.K., and Papike, J.J., 2004. Low abundances of highly siderophile elements in the lunar mantle: Evidence for prolonged late accretion. Earth and Planetary Science Letters **224**(3-4): 399-413.

Walker, R.J., and Stone, W.E., 2001. Os isotope constraints on the origin of the 2.7 Ga Boston Creek Flow, Ontario, Canada. Chemical Geology **175**(3-4): 567-579.

Warren, P.H. (2003). The Moon. Treatise on Geochemistry. Amsterdam, Elsevier. **1:** 559-599.

Warren, P.H., Jerde, E.A., and Kallemeyn, G.W., 1989. Lunar meteorites: siderophile element contents, and implications for the composition and origin of the Moon. Earth and Planetary Science Letters **91**(3): 245-260.

Willbold, M., Elliott, T., and Moorbath, S., 2011. The tungsten isotopic composition of the Earth's mantle before the terminal bombardment. Nature **477**(7363): 195-198.

Willbold, M., Mojzsis, S.J., Chen, H.W., and Elliott, T., 2015. Tungsten isotope composition of the Acasta Gneiss Complex. Earth and Planetary Science Letters **419**: 168-177.

Yin, Q., Jacobsen, S.B., Yamashita, K., Blichert-Toft, J., Telouk, P., and Albarede, F., 2002. A short timescale for terrestrial planet formation from Hf-W chronometry of meteorites. Nature **418**(6901): 949-952.

Figure captions

Fig. 1. Integrated schematic section of the Boston Creek Flow (BCF) sampled in this study. Samples J17 and 2-18 are from the Walker and Stone (2001) study. Shown are textural variations within the BCF, sample numbers, their location in the sequence, and MgO contents (wt. %).

Fig. 2. Abundances of selected major (wt. %) and lithophile trace (ppm) elements and W (ppb) obtained in this study plotted against MgO contents (wt. %) in the BCF. Highlighted in the W versus MgO diagram are the two sample powders from the Walker and Stone (2001) study analyzed here, which likely experienced W contamination during sample preparation. See text for additional details.

Fig. 3. a. BSE-normalized abundances of lithophile trace elements in the BCF arranged in decreasing order of incompatibility during mantle melting. The normalizing values for W are from (Arevalo and McDonough, 2008) and for the rest of the elements from (Hofmann, 1988); **b, c**. Diagrams of W/W* and μ^{182}W versus LOI (loss on ignition) for the BCF. Highlighted are two samples from the Walker and Stone (2001) study analyzed here, which likely experienced W contamination during sample preparation. Note the positive correlation between the index of alteration (LOI) and the magnitude of the W abundance anomaly likely indicating post-magmatic control on the W abundance variations in the BCF, and the lack thereof between the index of alteration and the magnitude of the positive ^{182}W anomaly likely indicating derivation of W from the BCF itself. See text for additional details.

Fig. 4. Re-Os isochron diagram for samples from the BCF analyzed in this study. Sample BC06 plots well above the regression line and was excluded from the ISOPLOT regression calculations. See text for additional details.

Fig. 5. CI chondrite-normalized HSE abundances in whole-rock samples from the BCF. Normalizing values are from (Horan *et al.*, 2003).

Fig. 6. Abundances of the highly siderophile elements in the BCF (ppb) obtained in this study plotted against MgO contents (wt. %).

Fig. 7. Tungsten isotopic compositions of samples from the BCF analyzed in this study. The data are reported in μ^{182}W units, which are part per million (ppm) deviations of the ^{182}W/^{184}W ratio of a given sample relative to the mean ^{182}W/^{184}W ratio measured for the Alfa Aesar W standard. Each symbol corresponds to a separately digested sample.

Fig. 8. Neodymium isotopic compositions of samples from the BCF analyzed in this study. The data are reported in μ^{142}Nd units, which are part per million (ppm) deviations of the ^{142}Nd/^{144}Nd ratio of a given sample relative to the mean ^{142}Nd/^{144}Nd ratio measured for the Nd standard AMES with an external precision of 2.8 ppm over the two-year period leading up to the present analytical campaign. Each symbol corresponds to a separately digested sample. Data for three separate digestions of the USGS GRM BCR-1 are reported for reference.

Fig. 9. (a) ^{147}Sm-^{143}Nd and **(b)** ^{176}Lu-^{176}Hf isochron diagrams for samples from the BCF analyzed in this study. See text for additional details. **(c)** Diagram illustrating the initial ε^{143}Nd and ε^{176}Hf values for the mantle source of the BCF and for the Chondritic Uniform Reservoir (CHUR) and Depleted MORB Mantle (DMM) calculated at the time of BCF

emplacement (2720 Ma). The CHUR and DMM parameters are from (Jacobsen and Wasserburg, 1980), (Bouvier *et al.*, 2008), and (Blichert-Toft and Puchtel, 2010). Note the coupled, or congruent, behavior between the two isotope systems in the source of the BCF resulting in the data plotting on the terrestrial array.

Fig. 10. Initial $^{187}Os/^{188}Os$ isotopic compositions, expressed in $\gamma^{187}Os$ terms, of the Archean komatiite systems plotted as a function of age. The data are from (Foster *et al.*, 1996; Puchtel *et al.*, 2004a; Puchtel *et al.*, 2005; Puchtel *et al.*, 2007; Puchtel *et al.*, 2009a; Puchtel *et al.*, 2009b; Puchtel *et al.*, 2014; Puchtel *et al.*, 2016a; Puchtel *et al.*, 2016b) and this study. The data for chondritic meteorites are compiled from (Walker *et al.*, 2002; Brandon *et al.*, 2005; Fischer-Gödde *et al.*, 2010).

Fig. 11. Calculated total Pt and Pd abundances in the sources of Archean komatiite systems plotted as *per cent* of the total Pt and Pd abundances in the estimates for modern BSE of (Becker *et al.*, 2006). The sources of the data are as follows. 2.41 Ga Vetreny Belt - (Puchtel *et al.*, 2016b); 2.69 Ga Belingwe - (Puchtel *et al.*, 2009b); 2.72 Ga Pyke Hill and Alexo - (Puchtel *et al.*, 2004b); 2.72 Ga Boston Creek - this study; 2.82 Ga Kostomuksha - (Puchtel and Humayun, 2005); 2.88 Ga Volotsk-Kamennoozero - (Puchtel *et al.*, 2007); 3.26 Ga Weltevreden and 3.48 Ga Komati - (Puchtel *et al.*, 2014); 3.55 Ga Schapenburg - (Puchtel *et al.*, 2016a). Uncertainties are 2SD. See text for additional details.

Fig. 12. $\mu^{182}W$ versus total calculated HSE abundances in the sources of Archean komatiite systems studied to-date relative to those in the estimates for the present-day BSE of (Becker *et al.*, 2006). This proportion corresponds to the fraction of the total HSE budget of the BSE added during late accretion assuming an HSE-free Earth mantle prior to late accretion. The $\mu^{182}W$ of the BSE prior to late accretion is constrained via ISOPLOT regression analysis of the $\mu^{182}W$ and HSE compositions of the BCF and the present-day BSE to be +18±7 ppm. The $\mu^{182}W$ for the lunar mantle of +25±5 ppm (Kruijer *et al.*, 2015; Touboul *et al.*, 2015) is identical to the estimate for the pre-late accretion Earth mantle, thus, providing further support to the notion that the Moon and Earth formed from material with identical ^{182}W compositions (Kleine and Walker, 2017). The W isotopic data and estimates of the total HSE contents for the komatiite systems are from (Puchtel and Humayun, 2005; Touboul *et al.*, 2012; Puchtel *et al.*, 2014; Puchtel *et al.*, 2016a; Puchtel *et al.*, 2016b), and this study.

1486 **Table 1.** Major (wt. %) and minor (ppm) element data for the USGS GRM BIR-1, BCR-1, and BHVO-2

Sample	BIR-1_1	BIR-1_2	BIR-1_3	BIR-1_4	BIR-1_5	Average (±2SD)	GeOReM (±2SE)	BCR-1	GeOReM (±2SE)	BHVO-2	GeOReM (±2SE)
SiO_2	47.1	47.2	47.2	46.8	47.0	47.1±0.4	47.8±0.2	53.9	54.5±0.5	48.9	49.6±0.1
TiO_2	0.946	0.939	0.945	0.947	0.965	0.948±0.020	0.959±0.007	2.28	2.24±0.04	2.69	2.73±0.02
Al_2O_3	15.5	15.5	15.6	15.3	15.3	15.5±0.2	15.5±0.1	13.8	13.6±0.1	13.5	13.4±0.1
Fe_2O_3	11.2	11.5	11.5	11.5	11.4	11.4±0.2	11.4±0.1	13.6	13.4±0.2	12.6	12.4±0.1
MnO	0.180	0.170	0.157	0.172	0.190	0.174±0.025	0.173±0.002	0.201	0.183±0.003	0.150	0.169±0.002
MgO	9.70	9.57	9.86	9.71	9.69	9.71±0.20	9.69±0.05	3.69	3.47±0.04	7.44	7.26±0.04
CaO	13.3	13.1	13.4	13.3	13.2	13.3±0.2	13.3±0.1	7.17	7.12±0.22	11.5	11.4±0.1
Na_2O	1.78	1.79	1.85	1.91	1.80	1.83±0.11	1.83±0.02	3.22	3.33±0.05	2.20	2.22±0.05
K_2O	0.010	0.012	0.015	0.010	0.008	0.011±0.01	0.029±0.003	1.80	1.73±0.02	0.478	0.513±0.004
P_2O_5	0.025	0.028	0.021	0.019	0.016	0.022±0.010	0.030±0.004	0.36	0.36±0.01	0.253	0.269±0.005
Total	99.78	99.83	100.54	99.62	99.63	99.88	100.70	99.91	99.96	99.68	99.99
LOI	-0.35	-0.31	-0.33	-0.06	-0.48	-0.31		0.37		-0.33	
Cr	417	417	409	382	384	402±35	393±4	16	14±1	314	287±3
Ni	140	134	145	159	146	145±19	169±2	15	12±1	144	120±1

1487
1488

1489 **Table 2.** HSE abundances (in ppb) and Os isotopic data for the SRM MUH-1, OKUM, and TDB-1.

Sample	Re	Os	Ir	Ru	Pt	Pd	$^{187}Os/^{188}Os$
MUH-1	0.183	3.42	3.65	6.90	8.25	8.10	0.12728±6
OKUM	0.471	0.722	0.813	4.40	12.6	11.5	0.27781±14
TDB-1	0.788	0.109	0.0606	0.204	4.89	21.5	1.1543±9
MUH-1 reference	0.182	4.13	3.78	7.23	9.76	8.88	0.1280
2SD	0.047	2.95	1.22	0.87	3.01	1.36	0.0034
OKUM reference	0.499	0.847	1.00	4.66	11.8	11.5	0.2666
2SD	0.076	0.24	0.26	1.12	2.9	2.1	0.0090
TDB-1 reference[1]	0.795	0.117	0.0744	0.198	5.01	24.4	0.916
2SD	0.045	0.022	0.0188	0.017	0.36	3.8	0.195
TDB-1 reference[2]	1.01	0.106	0.059	0.231	4.74	22.3	0.973
2SD	0.07	0.020	0.011	0.079	1.19	3.7	0.128

1490 The MUH-1 and OKUM reference values are from Burnham *et al.* (2010) and the TDB-1 reference values
1491 are from [1](Meisel and Moser, 2004) and [2](Dale *et al.*, 2012).
1492

Table 3. Major (wt. %) and minor (ppm) element data for the Boston Creek Flow

Sample	BC01	BC02	BC03	BC06	BC07	BC08	BC09	BC10	J17_1	J17	2-18
SiO_2	44.6	46.8	47.4	44.7	40.6	38.4	40.8	39.6	40.9	40.7	41.5
TiO_2	1.376	1.335	1.368	1.238	0.628	0.415	0.632	0.486	0.480	0.470	0.531
Al_2O_3	7.89	7.65	8.00	6.98	3.06	2.04	3.07	2.34	2.38	2.36	2.76
Fe_2O_3	19.3	17.5	18.3	19.2	22.1	20.1	22.2	20.8	18.0	17.7	18.0
MnO	0.263	0.244	0.247	0.326	0.306	0.319	0.316	0.298	0.249	0.248	0.242
MgO	8.26	8.88	8.17	13.4	28.5	34.0	28.8	32.1	32.8	33.4	31.8
CaO	16.63	14.42	13.74	13.10	4.13	3.50	3.50	3.63	4.08	4.00	3.96
Na_2O	1.92	2.27	2.43	0.63	0.10	0.08	0.11	0.08	0.04	0.04	0.06
K_2O	0.216	0.162	0.190	0.136	0.009	0.006	0.006	0.000	0.000	0.000	0.001
P_2O_5	0.083	0.088	0.088	0.071	0.034	0.035	0.032	0.026	0.030	0.030	0.040
Total	100.53	99.38	99.85	99.79	99.52	98.91	99.38	99.40	98.90	98.96	98.96
LOI	5.82	2.99	1.57	3.61	6.73	11.31	6.56	7.89	8.58	8.47	8.29
Cr	559	586	440	746	2261	4443	2180	3685	4709	4669	3762
Ni	247	213	181	397	1914	3166	2062	2790	2922	2505	3449
Al_2O_3/TiO_2	5.7	5.7	5.8	5.6	4.9	4.9	4.9	4.8	5.0	5.0	5.2

Note. Analyses were re-calculated on an anhydrous basis, but not re-normalized to 100% in order to preserve information on the quality of the analyses.

Table 4. Trace element data (ppm) for the Boston Creek Flow

Sample	BC01	BC02	BC03	BC06	BC07	BC08	*Replicate*	BC09	BC10	*Replicate*	J17_1	J17	2-18	*Replicate*
Th	0.936	0.936	0.940	0.851	0.384	0.273	0.268	0.372	0.295	0.283	0.304	0.315	0.344	0.340
U	0.263	0.264	0.259	0.231	0.115	0.0787	0.0747	0.106	0.0833	0.0782	0.0831	0.0873	0.0962	0.0980
Nb	11.1	10.4	10.4	9.35	4.46	3.32	3.38	4.17	3.37	3.40	3.88	3.92	4.09	4.08
La	11.7	11.8	12.1	9.87	4.69	3.16	3.22	4.46	3.59	3.60	3.76	3.54	3.89	3.70
Ce	28.5	27.7	27.6	24.3	12.9	7.78	7.86	12.71	9.07	8.90	9.09	9.19	10.9	10.5
Pr	3.96	4.06	4.12	3.32	1.66	1.14	1.11	1.66	1.17	1.16	1.38	1.42	1.66	1.59
Nd	16.9	17.3	17.5	14.3	7.03	4.75	4.65	6.91	5.56	5.49	5.88	5.90	6.34	6.24
Sm	3.77	3.87	3.88	3.30	1.54	1.02	1.00	1.51	1.24	1.19	1.26	1.27	1.41	1.37
Hf	2.00	1.99	1.96	1.74	0.766	0.527	0.477	0.836	0.647	0.620	0.575	0.556	0.664	0.650
Zr	67.2	63.7	64.7	59.9	27.1	17.6	16.9	27.2	19.3	20.8	20.4	19.7	21.4	21.4
Eu	1.26	1.22	1.26	1.05	0.449	0.333	0.321	0.405	0.349	0.339	0.394	0.408	0.407	0.412
Gd	3.82	3.90	4.01	3.44	1.57	1.00	0.957	1.53	1.14	1.11	1.23	1.23	1.38	1.38
Tb	0.553	0.564	0.567	0.517	0.230	0.142	0.136	0.222	0.165	0.158	0.172	0.172	0.200	0.202
Dy	3.35	3.32	3.35	3.11	1.35	0.830	0.806	1.35	0.975	0.947	1.01	1.02	1.17	1.19
Y	15.8	15.5	16.1	14.8	6.25	3.87	3.64	6.43	4.72	4.45	4.51	4.58	5.17	5.07
Ho	0.642	0.646	0.655	0.608	0.263	0.162	0.155	0.262	0.192	0.184	0.192	0.193	0.222	0.224
Er	1.76	1.78	1.79	1.67	0.725	0.442	0.423	0.722	0.535	0.508	0.515	0.514	0.605	0.598
Tm	0.248	0.244	0.254	0.230	0.104	0.0623	0.0594	0.102	0.0725	0.0693	0.0701	0.0711	0.0829	0.0826
Yb	1.55	1.57	1.63	1.49	0.661	0.398	0.384	0.651	0.468	0.445	0.451	0.457	0.531	0.532
Lu	0.227	0.225	0.231	0.2159	0.0944	0.0585	0.0569	0.0951	0.0659	0.0638	0.0650	0.0662	0.0779	0.0788
Ti/Zr	123	126	127	124	139	142	147	139	151	140	141	143	149	149
Nb/Nb*	1.21	1.14	1.12	1.17	1.20	1.29	1.32	1.17	1.18	1.22	1.31	1.34	1.28	1.32
$(La/Sm)_N$	1.95	1.92	1.95	1.88	1.92	1.96	2.02	1.86	1.82	1.90	1.87	1.76	1.74	1.70
$(Gd/Yb)_N$	1.99	2.01	1.99	1.87	1.92	2.02	2.01	1.90	1.98	2.02	2.20	2.16	2.09	2.10

Note. Analyses were recalculated on an anhydrous basis.
N- normalized to the BSE values of (Hofmann, 1988).

Table 5. HSE abundances (ppb), Re-Os isotopic data, and elemental ratios for the Boston Creek Flow

Sample	Re	Os	Ir	Ru	Pt	Pd	$^{187}Re/^{188}Os$	$^{187}Os/^{188}Os$	$\gamma^{187}Os(T)$	$(Os/Ir)_N$	$(Ru/Ir)_N$	$(Pd/Ir)_N$
BC02	1.061	0.08087	0.201	0.838	6.94	8.37	101.7±0.9	4.8334±50	+7.8	0.390	2.85	32.6
BC03	0.1678	0.04221	0.188	0.576	7.09	8.50	21.61±0.25	1.1180±6	+7.3	0.217	2.09	35.3
BC06	0.5516	0.07389	0.185	0.825	6.16	7.44	47.82±0.37	2.6668±11	+315	0.386	3.04	31.3
BC08	0.04416	0.3792	0.397	5.52	2.97	2.84	0.5619±0.0034	0.13798±6	+3.3	0.926	9.50	5.60
BC08 replicate	0.04436	0.3687	0.395	5.51	2.99	2.77	0.5806±0.0035	0.13860±8	+3.0	0.906	9.54	5.48
BC09	0.1193	0.1644	0.338	4.46	3.91	4.34	3.573±0.024	0.29284±17	+17	0.472	9.01	10.0
BC10	0.1127	0.3958	0.780	7.46	3.05	3.51	1.382±0.008	0.18112±8	+8.0	0.492	6.54	3.51
BC10 replicate	0.1138	0.3979	0.749	7.39	3.02	3.16	1.388±0.008	0.18199±13	+8.5	0.515	6.74	3.30
J17_1	0.04875	2.354	1.94	6.94	3.25	3.26	0.0996±0.0006	0.11356±5	+0.52	1.18	2.45	1.32
J17_1 replicate	0.04803	2.321	1.88	6.45	3.38	3.29	0.0995±0.0006	0.11352±6	+0.48	1.20	2.34	1.37
J17	0.07042	2.233	1.82	6.76	3.25	3.27	0.1517±0.0009	0.11334±4	-1.9	1.19	2.54	1.40
Corrected*	*0.04421*	2.233					*0.1033±0.0006*	0.11334±4	+0.15			
J17 replicate	0.07155	2.367	1.89	6.50	3.34	3.25	0.1454±0.0009	0.11305±5	-1.9	1.21	2.35	1.34
Corrected*	*0.04492*	2.367					*0.0990±0.0006*	0.11305±5	+0.07			
2-18	0.08796	2.973	2.47	6.26	3.23	3.67	0.1423±0.0009	0.11450±3	-0.44	1.17	1.74	1.16
2-18 replicate	0.08643	2.946	2.38	5.63	3.31	3.66	0.1411±0.0008	0.11450±5	-0.39	1.20	1.61	1.20
J17**	0.09310	2.245					0.200±0.005	0.11418±5	-3.2			
J17 replicate**	0.09495	2.076					0.217±0.005	0.11420±5	-3.9			
2-18**	0.1379	2.924					0.227±0.007	0.11509±5	-3.5			

Note. The HSE abundances were re-calculated on an anhydrous basis. The initial $\gamma^{187}Os$ values were calculated for $T = 2720$ Ma using the parameters specified in the text. Sample **BC06** plots well above the isochron and was not included in the regression calculations. The HSE normalizing values are from (Horan *et al.*, 2003). *Re abundance corrected for estimated 46% Re contamination during sample preparation in the (Walker and Stone, 2001) study. **Data from the Walker and Stone (2001) study. Samples **J17** and **2-18** are the same sample powders analyzed here and by Walker and Stone (2001), whereas sample **J17_1** is a new powder prepared in this study using uncrushed sample **J17** from the Walker and Stone (2001) study and metal-free equipment. Note the ~50% higher Re abundances obtained for the sample powder **J17** by Walker and Stone (2001) compared to this study, and also ~46% higher Re abundances in the sample powder **J17** relative to **J17_1** obtained in this study.

Table 6. Tungsten abundances (in ppb) and W isotopic compositions of the Boston Creek Flow

Sample	W (±2SE)	μ^{182}W (±2SE)
BC01	385±4	+7.6±2.1
Replicate	392±5	+7.4±4.8
BC02	346±3	+18.5±3.2
Replicate	344±5	+15.2±2.4
BC03	249±3	+14.6±3.4
Replicate	245±4	
BC06	469±5	+11.2±3.1
Replicate	485±6	
BC07	626±6	+11.2±6.4
Replicate	618±7	+13.6±3.1
BC08	462±4	+10.6±2.7
Replicate	458±6	
BC09	811±8	+9.3±2.1
Replicate	815±9	+7.2±3.1
BC10	319±3	+13.9±3.3
Replicate	313±5	
J17_1	347±5	
J17	1305±13	
2-18	675±7	

Note. Abundances were re-calculated on an anhydrous basis. Uncertainties on W isotopic compositions for individual samples are the 2SE in-run statistics of the individual analyses. Samples **J17** and **2-18** are the powders from the Walker and Stone (2001) study, whereas sample **J17_1** is the new powder prepared in this study using un-crushed material for sample **J17** and metal-free equipment. Note ~4× higher W abundances in **J17** compared to **J17_1** likely due to W contamination of the sample during processing in metal in the Walker and Stone (2001) study, also consistent with ~50% higher Re abundance in that powder. Sample **2-18**, which has ~2× higher W abundances than **J17_1**, is also likely contaminated with W (and probably Re) during processing in metal in the Walker and Stone (2001) study.

Table 7. Sm-Nd isotope and concentration data for the Boston Creek Flow and the USGS GRM BCR-1

Sample	$^{147}Sm/^{144}Nd$	±2SE	$^{143}Nd/^{144}Nd$	±2SE	$\varepsilon^{143}Nd(T)$	$\mu^{142}Nd$
BC01	0.1349	0.0007	0.511655	0.000001	+2.5	−4.4±1.9
BC02	0.1344	0.0007	0.511637	0.000001	+2.3	−1.9±2.0
Replicate*	0.1332	0.0007	0.511632	0.000001	+2.6	−3.8±1.5
BC03	0.1344	0.0007	0.511652	0.000001	+2.6	−1.0±1.7
Replicate*	0.1347	0.0007	0.511649	0.000002	+2.4	−1.9±3.5
BC06	0.1390	0.0007	0.511727	0.000001	+2.4	−5.6±2.1
Replicate*	0.1382	0.0007	0.511717	0.000001	+2.5	−3.8±1.6
BC08	0.1306	0.0007	0.511573	0.000001	+2.4	−5.5±2.2
Replicate*	0.1303	0.0007	0.511579	0.000001	+2.6	−2.0±2.5
BC09	0.1317	0.0007	0.511608	0.000001	+2.7	−6.1±2.1
Replicate*	0.1331	0.0007	0.511624	0.000001	+2.5	−4.6±2.1
BC10	0.1333	0.0007	0.511635	0.000001	+2.6	−5.5±1.7
Replicate*	0.1339	0.0007	0.511638	0.000001	+2.5	−4.4±2.8
J-17	0.1302	0.0007	0.511573	0.000001	+2.5	−5.3±2.1
2-18	0.1291	0.0006	0.511548	0.000001	+2.4	−1.9±2.0
BCR-1			0.512645	0.000002		+1.1±2.5
Replicate*			0.512645	0.000001		+0.3±1.7
Replicate*			0.512644	0.000002		+0.7±3.6

Note. *Replicate digestions of the samples. The $^{147}Sm/^{144}Nd$ ratios were determined on ~3% solution aliquots of the same sample digestions performed for the high-precision Nd isotopic analyses, using the SA ICP-MS technique, as specified in the text. Due to the lack of knowledge of the precise weight of the sample represented by the solution aliquots, only the Sm/Nd ratios are reported here. Initial $\varepsilon^{143}Nd$ values were calculated for the age $T = 2720$ Ma using the parameters specified in the text. The data for the USGS GRM BCR-1 were obtained on three separate digestions over the course of the entire analytical campaign.

Table 8. Lu-Hf isotope and concentration data for the Boston Creek komatiites

Sample	Lu (ppm)	Hf (ppm)	$^{176}Lu/^{177}Hf$	±2SE	$^{176}Hf/^{177}Hf$	±2SE	$\varepsilon^{176}Hf(T)$
BC02	0.2161	1.713	0.01790	0.00004	0.282069	0.000007	+3.6
BC03	0.2218	1.761	0.01787	0.00004	0.282077	0.000008	+4.0
BC06	0.2020	1.585	0.01809	0.00004	0.282094	0.000006	+4.2
BC08	0.05095	0.4189	0.01726	0.00003	0.282064	0.000018	+4.6
BC09	0.08686	0.6903	0.01786	0.00004	0.282098	0.000008	+4.7
BC10	0.05915	0.4195	0.02001	0.00004	0.282188	0.000014	+4.0

Note. Initial $\varepsilon^{176}Hf$ values were calculated for the age $T = 2720$ Ma, using the parameters specified in the text.

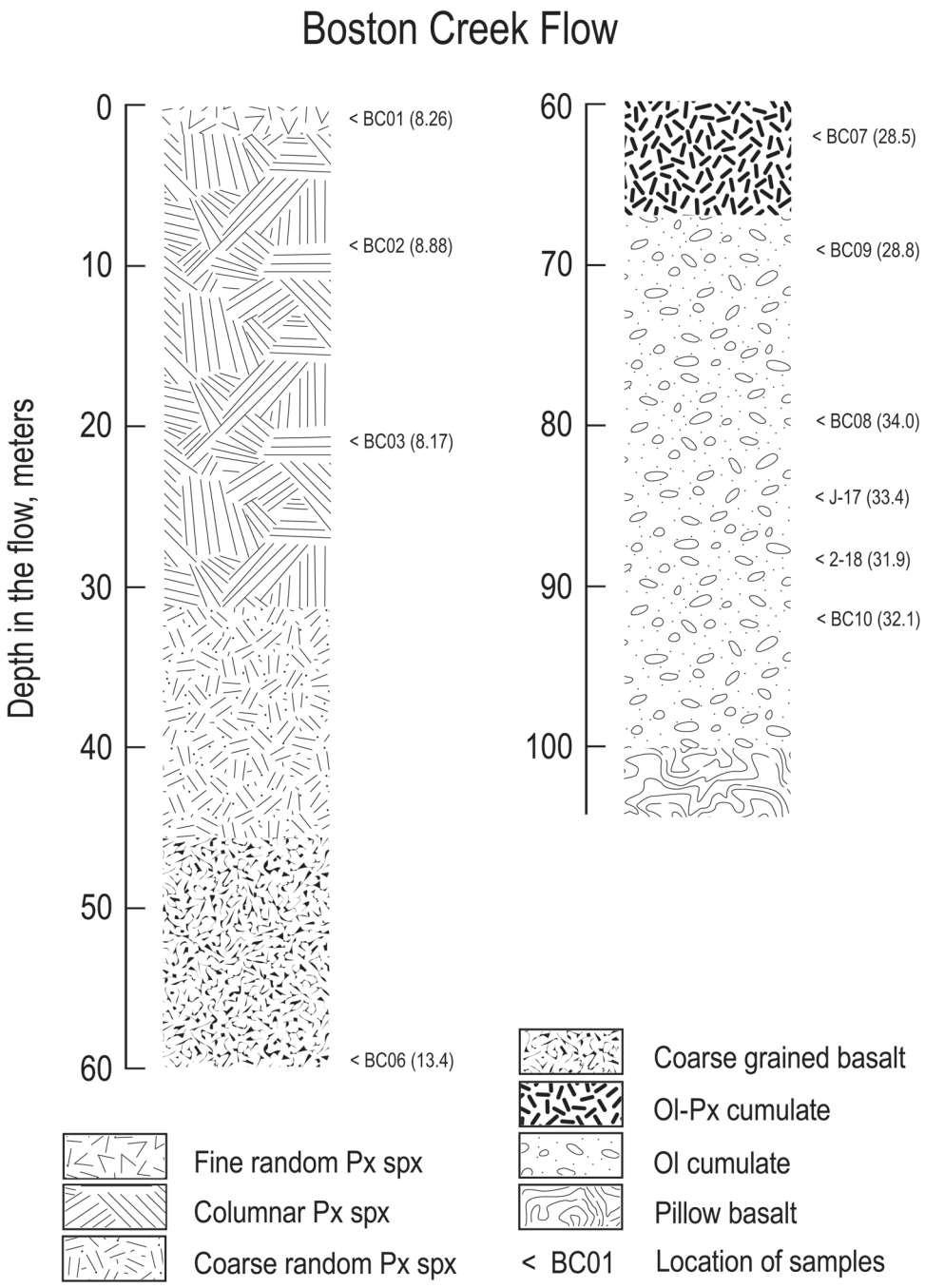

1539

1540 **Fig. 1.**

1541

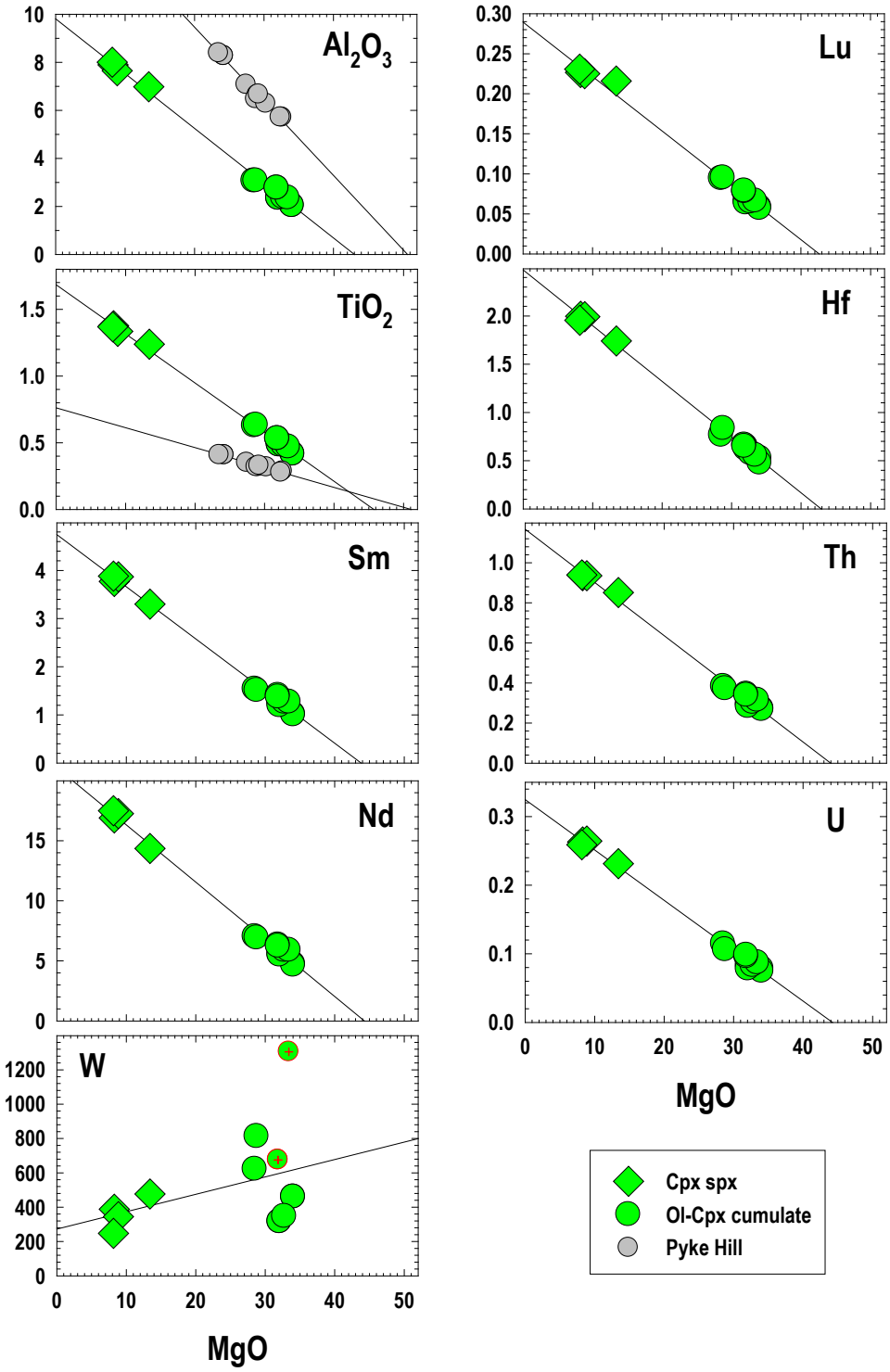

1542

1543 **Fig. 2.**

1544

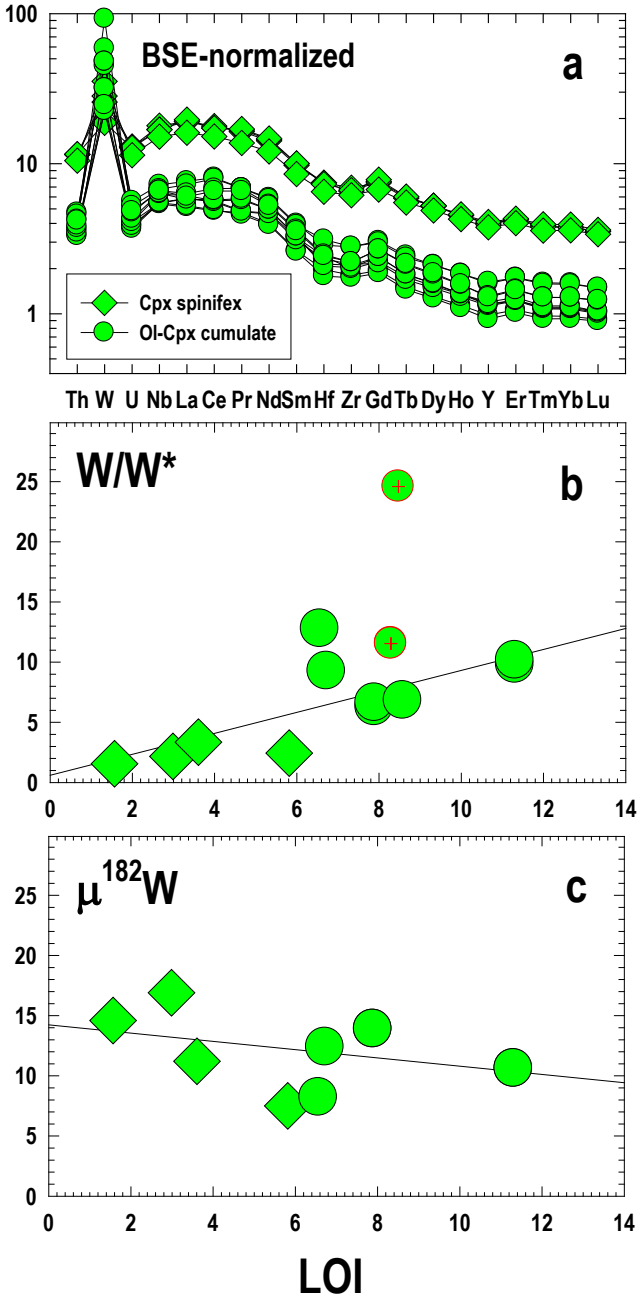

1545

1546 **Fig. 3.**

1547

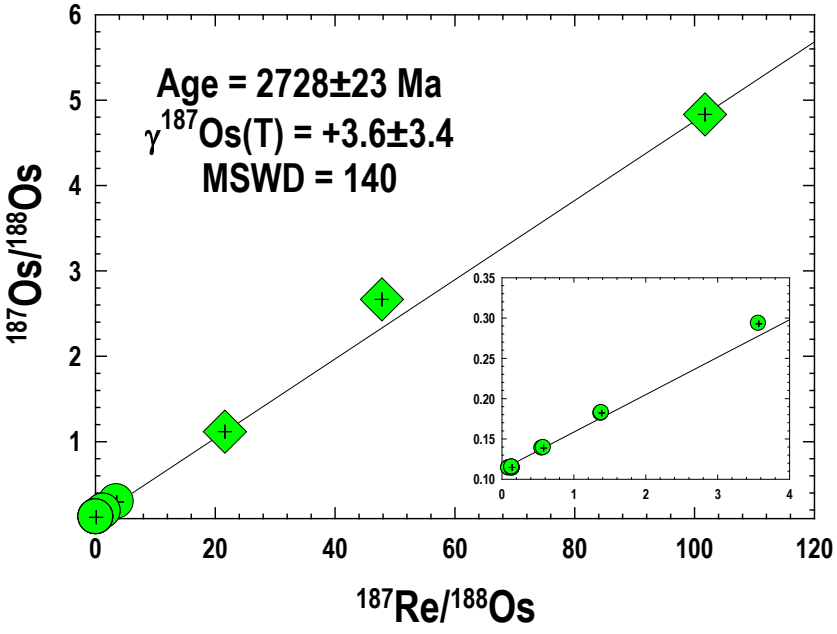
Age = 2728±23 Ma
γ187Os(T) = +3.6±3.4
MSWD = 140
187Os/188Os
187Re/188Os
0
20
40
60
80
100
120
1
2
3
4
5
6
0.10
0.15
0.20
0.25
0.30
0.35

Fig. 4.

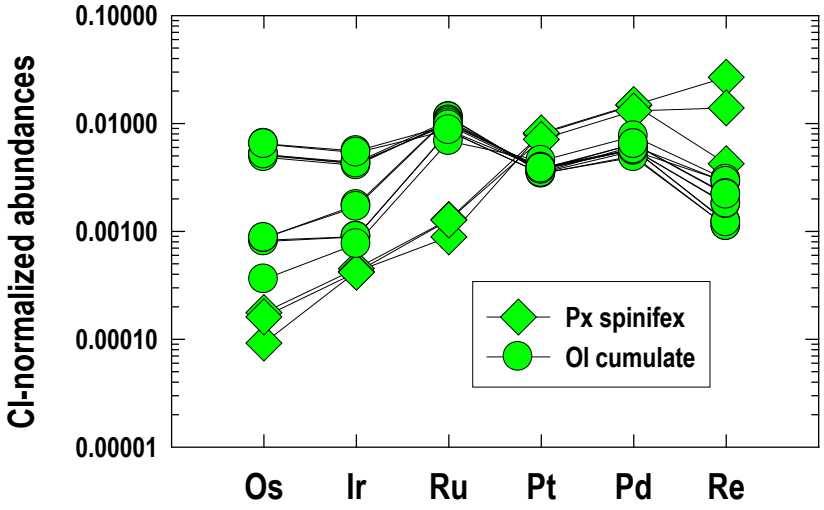

1552
1553 **Fig. 5.**

1554

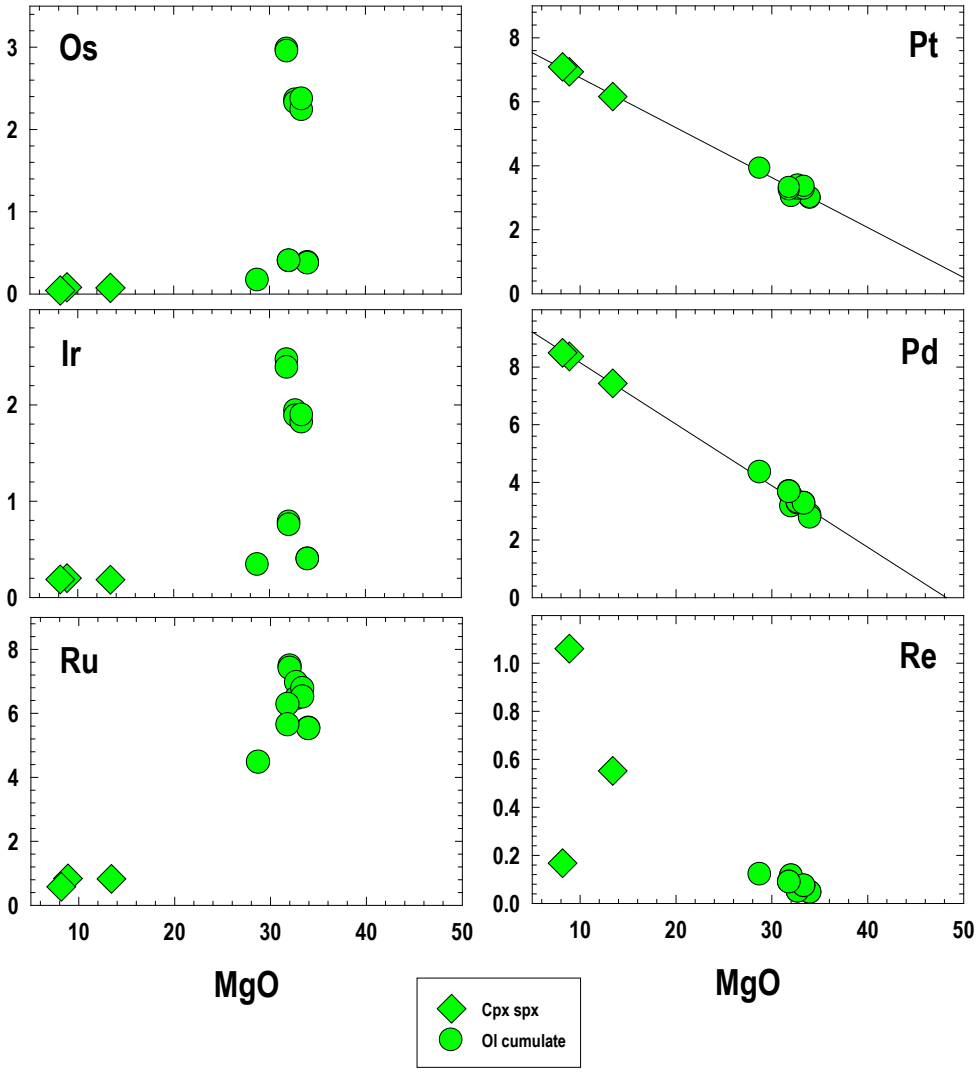

1555

1556 **Fig. 6.**

1557

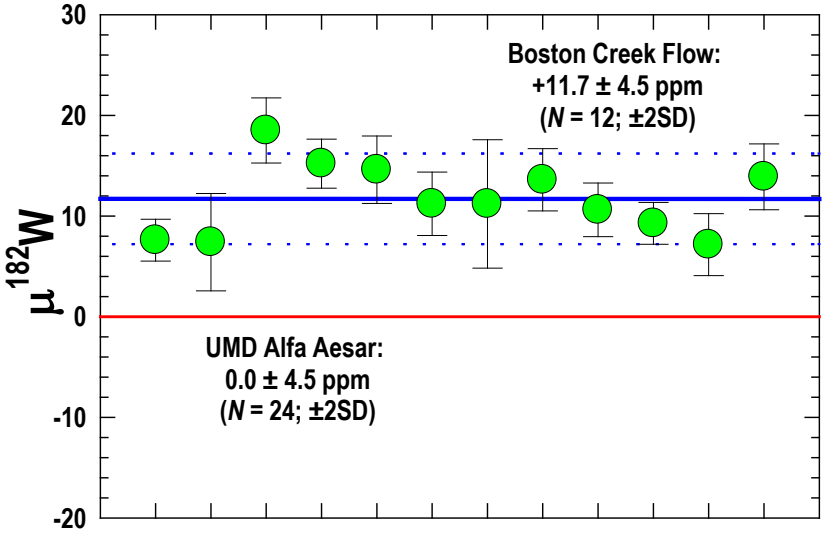

1558

1559 **Fig. 7.**

1560

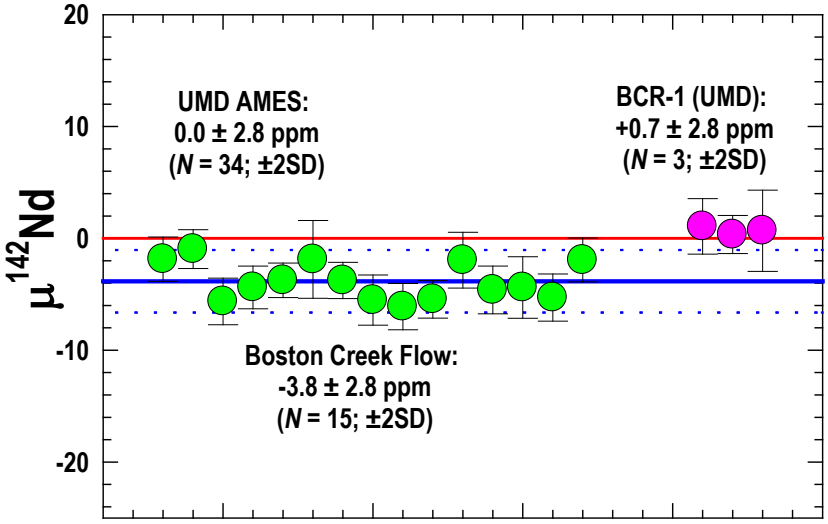
20
10
0
-10
-20
μ142Nd
UMD AMES:
0.0 ± 2.8 ppm
(N = 34; ±2SD)
BCR-1 (UMD):
+0.7 ± 2.8 ppm
(N = 3; ±2SD)
Boston Creek Flow:
-3.8 ± 2.8 ppm
(N = 15; ±2SD)

Fig. 8.

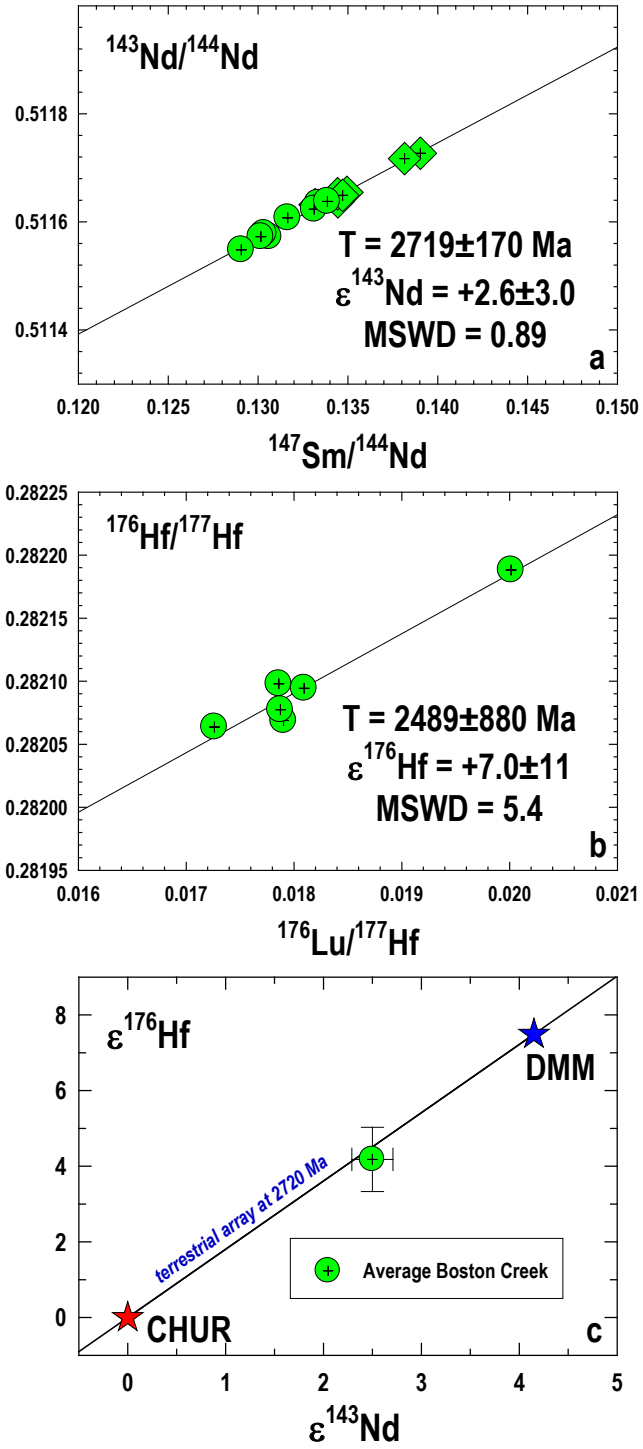

1564
1565 **Fig. 9.**
1566

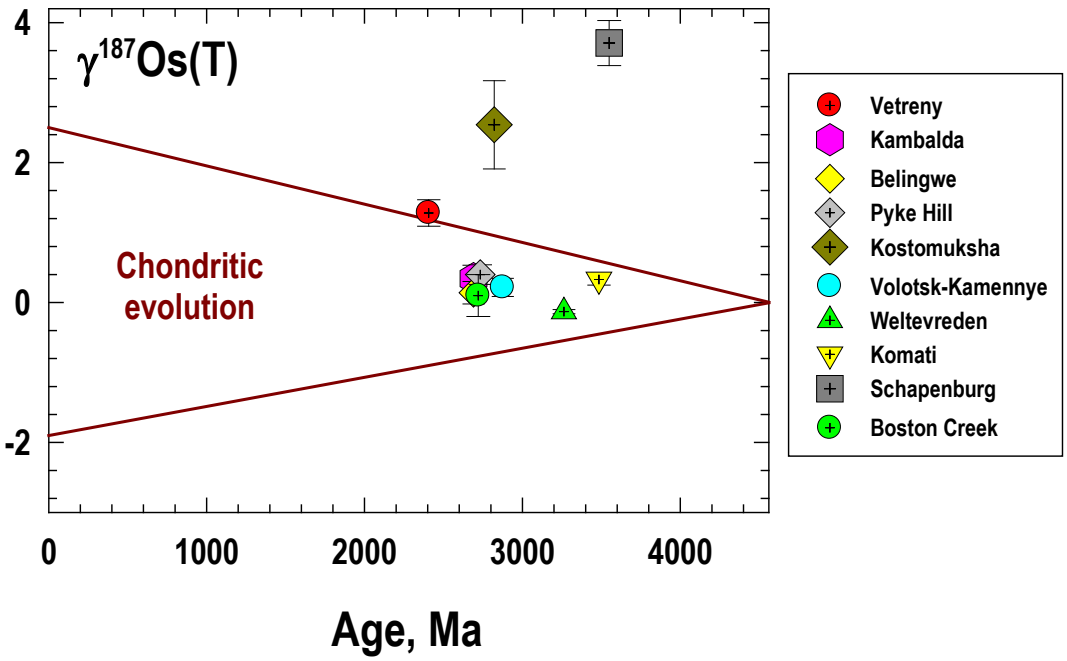
γ187Os(T)
Chondritic
evolution
4
2
0
-2
0
1000
2000
3000
4000
Age, Ma
Vetreny
Kambalda
Belingwe
Pyke Hill
Kostomuksha
Volotsk-Kamennye
Weltevreden
Komati
Schapenburg
Boston Creek

Fig. 10.

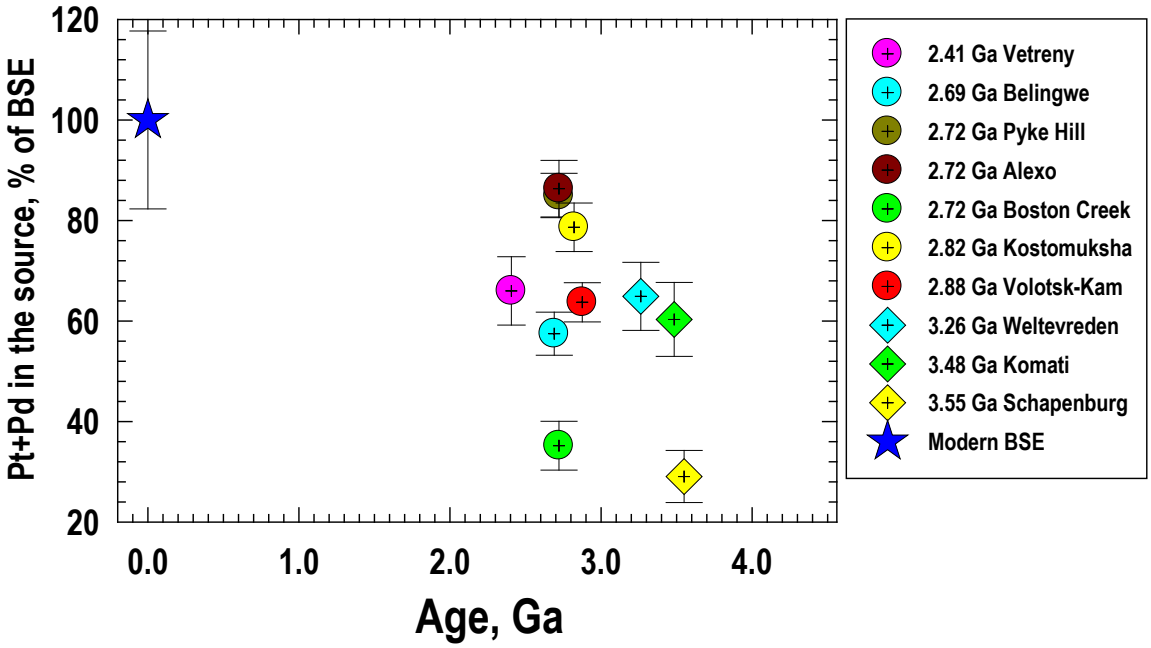
Pt+Pd in the source, % of BSE
120
100
80
60
40
20
0.0
1.0
2.0
3.0
4.0
Age, Ga
2.41 Ga Vetreny
2.69 Ga Belingwe
2.72 Ga Pyke Hill
2.72 Ga Alexo
2.72 Ga Boston Creek
2.82 Ga Kostomuksha
2.88 Ga Volotsk-Kam
3.26 Ga Weltevreden
3.48 Ga Komati
3.55 Ga Schapenburg
Modern BSE

Fig. 11.

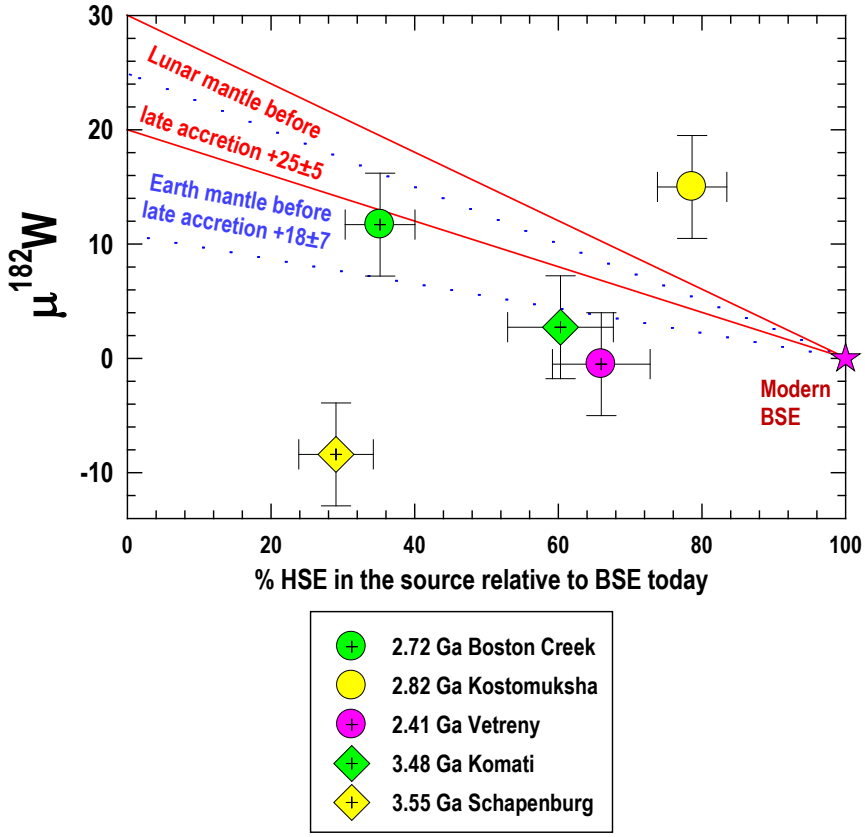

1573
1574 **Fig. 12.**
1575